

# UBVR AND HST MID-UV AND NEAR-IR SURFACE PHOTOMETRY AND RADIAL COLOR GRADIENTS OF LATE-TYPE, IRREGULAR, AND PECULIAR GALAXIES.

VIOLET A. TAYLOR<sup>1</sup>, ROLF A. JANSEN<sup>1</sup>, ROGIER A. WINDHORST<sup>1</sup>  
Department of Physics and Astronomy, Arizona State University, Tempe, AZ 85287

STEPHEN C. ODEWAHN<sup>2</sup>  
McDonald Observatory, University of Texas at Austin, Austin, TX 78712

AND

JOHN E. HIBBARD<sup>3</sup>  
National Radio Astronomy Observatory, 520 Edgemont Road, Charlottesville, VA 22903  
*Draft version June 2, 2005*

## ABSTRACT

We introduce a dataset of 142 mostly late-type spiral, irregular, and peculiar (interacting or merging) nearby galaxies observed in *UBVR* at the Vatican Advanced Technology Telescope (VATT), and present an analysis of their radial color gradients. We confirm that nearby elliptical and early- to mid-type spiral galaxies show either no or only small color gradients, becoming slightly bluer with radius. In contrast, we find that late-type spiral, irregular, peculiar, and merging galaxies become on average redder with increasing distance from the center. The scatter in radial color gradient trends increases toward later Hubble type. As a preliminary analysis of a larger data-set obtained with the *Hubble Space Telescope (HST)*, we also analyze the color gradients of six nearby galaxies observed with NICMOS in the near-IR (*H*) and with WFPC2 in the mid-UV (F300W) and red (F814W). We discuss the possible implication of these results on galaxy formation and compare our nearby galaxy color gradients to those at high redshift. We present examples of images and *UBVR* radial surface brightness and color profiles, and of the tables of measurements; the full atlas and tables are published in the electronic edition only.

*Subject headings:* galaxies: fundamental parameters – galaxies: interactions – galaxies: peculiar – galaxies: irregular – galaxies: spiral – galaxies: photometry

## 1. INTRODUCTION

Technological advances such as space-based telescopes like the *Hubble Space Telescope (HST)* have expanded our view of the Universe to higher redshifts than ever before, giving us the opportunity to look back in time to the earliest stages of galaxy development to determine the mechanisms of galaxy assembly and how galaxies evolved into what we see in the present-day Universe. Since the optical and near-IR light of high redshift galaxies observed with *HST* was emitted in the rest-frame far- to mid-UV (“band-pass shifting”), an understanding of the fundamental UV properties of galaxies in general is crucial to our understanding of these high redshift galaxies. The vast majority of galaxies in the Hubble Deep Field (HDF) appear to have characteristics resembling local irregular and peculiar/merging galaxies (e.g., Driver et al. 1995, 1998; Glazebrook et al. 1995; Abraham et al. 1996; Odewahn et al. 1996; Ellis 1997), although it is difficult to distinguish these classes at lower linear spatial resolution. Size-luminosity evolution studies show that, at the same luminosity, high redshift galaxies are more compact and less massive than nearby galaxies, as measured in both the UV and optical rest-frames (Giavalisco et al. 1996; Lowenthal et al. 1997; Ferguson et al. 2004; Trujillo et al. 2004). They show that high redshift galaxies are inherently different from nearby luminous galaxies, regardless of band-pass shifting effects.

Therefore, the resemblance of high redshift galaxies to nearby lower-luminosity irregular and peculiar/merging galaxies may be real, and studying stellar population distributions of nearby irregular and peculiar/merging galaxies may provide further understanding of high redshift galaxies, and hence of galaxy formation and evolution.

Radial color gradients can provide an indication of stellar population or metallicity distribution differences between the inner and outer regions of a galaxy (as modulated by dust), and can constrain certain mechanisms for how a galaxy assembled and subsequently evolved to its present state (Tinsley & Larson 1978; de Jong 1996). There have been several studies of the optical color gradients of sizable samples of nearby field galaxies. These include (but are not limited to) color gradients of early-type galaxies measured by Vader et al. (1988) from 35 elliptical and early-type spirals in *B–R*, by Franx et al. (1989) from 17 ellipticals in *U–R* and *B–R*, by Peletier et al. (1990) from 39 ellipticals in *U–R* and *B–R*, and by Tamura & Ohta (2003) from 51 rich galaxy cluster E and S0 galaxies in *B–R*. All four of these relatively large samples found that ellipticals either become bluer with radius or are constant in color, with color gradients that are generally interpreted as metallicity gradients.

Large studies of later-type galaxy color gradients were conducted by several other authors, such as Balcells & Peletier (1994), who measured color gradients from the bulges of 45 early-type spirals in *UBVRI*. De Jong

(1996) determined the color gradients of 86 face-on spiral galaxies in *BVR IHK*, and Tully et al. (1996) did so for 79 galaxies in the Ursa Major cluster. Jansen et al. (2000) determined  $U - B$  and  $B - R$  color differences between the inner and outer regions of a sample of 196 galaxies of all Hubble types. Bell & de Jong (2000) found stellar population and metallicity gradients for their 121 spiral galaxies, and MacArthur et al. (2004) analyzed color gradients and stellar population and metallicity gradients for these plus 51 other galaxies, including some irregular galaxies. All of these studies confirm the earlier finding (e.g., Sandage 1972; Persson, Frogel & Aaronson 1979) that spiral galaxies tend to get bluer with increasing radius. These color gradients were found to be mainly caused by stellar population gradients (de Jong 1996; Bell & de Jong 2000; MacArthur et al. 2004). Tully et al. (1996) and Jansen et al. (2000) find that low-luminosity ( $M_B > -17$  mag), often late-type/irregular galaxies are equally likely to become bluer or redder outward. Since there is no plausible galaxy formation theory that predicts positive metallicity gradients (Vader et al. 1988), these redder outer parts are most likely due to stellar age effects or dust. Jansen et al. (2000) find that the low-luminosity galaxies that are bluer in their central regions tend to have strong central  $H\alpha$  emission, supporting the hypothesis that the color gradients in these galaxies are due to a few star forming regions dominating the local colors. In more luminous massive galaxies, a single star forming region cannot dominate the azimuthally averaged colors and, hence, the observed color gradients reflect either systematically younger populations or systematically less extinction by dust at larger distances from the center. The presence of a bulge is likely to enhance such color gradients.

Due to significant atmospheric extinction and the poor response of most older thick CCD detectors below the Balmer break, large studies of the near-UV properties of galaxies, especially of the fainter irregular galaxies which seem to be analogs of the majority of high redshift galaxies, have not been feasible until the recent advent of large format UV sensitive detectors in space, such as on the balloon-born FOCA telescope (Milliard et al. 1992), sounding rocket and Astro/UIT flights (Bohlin et al. 1991; Hill et al. 1992; Kuchinski et al. 2000; Marcum et al. 2001), and HST/WFPC2 (Windhorst et al. 2002). The overall UV properties of galaxies in general, and of faint late-type galaxies in particular, is still rather poorly understood. Mid-UV and, to a lesser extent,  $U$ -band data are particularly useful for color gradient analysis: because the UV is more sensitive to changes in age and metallicity, color gradients will be more apparent. A color gradient will be more significant with a longer base-line in wavelength coverage between the two filters used, such that it is most useful to obtain equally deep images in filters at both mid-UV and near-IR wavelengths. Additionally, data at intermediate wavelengths are necessary to properly sample a large range of stellar populations. The high resolution of *HST* mid-UV and  $I$  images allow us to resolve individual stars or associations, which provides further, more detailed information about the distribution of metallicity and stellar populations within a galaxy. The addition of  $H$ -band *HST* images removes some of the dust degeneracy in a color analysis, considerably improving stellar population mea-

surements over optical colors alone (Cardiel et al. 2003).

In order to address the deficit of published color gradient studies for a large, homogeneous sample of irregular, peculiar, and merging galaxies across a large range of optical wavelengths, we present a data-set of 142 galaxies observed at the Vatican Advanced Technology Telescope (VATT) in (*UBVR*). We also present supplemental *HST* mid-UV and near-IR data for six galaxies. We discuss these datasets in Section 2 and describe the data analysis in Section 3. In Section 4 we discuss our results, complementing the findings of previous studies and increasing the database of color gradients to include a larger sample of irregular and peculiar/merging galaxies. In Section 5 we compare our results to those of the high-redshift universe, and discuss possible implications on galaxy formation and evolution.

## 2. DATA ACQUISITION AND REDUCTION

### 2.1. Sample Selection

We selected 82 galaxies from the RC3 (de Vaucouleurs et al. 1991) with (1) types later than or equal to Sd (de Vaucouleurs type  $7 \leq T \leq 10$ ), (2) sizes small enough to comfortably fit within the  $\sim 6.4'$  FOV of the VATT imager (to ensure accurate subtraction of the sky background), and (3)  $B$ -band surface brightness<sup>1</sup> brighter than  $\mu_B = 25$  mag arcsec<sup>-2</sup>, to ensure efficient imaging at the VATT and with HST. The median diameter of the galaxies in this sample is  $\sim 1.4'$ , and the median surface brightness is  $\sim 23.0$  mag arcsec<sup>-2</sup>. We supplemented this sample with 23 galaxies from the list of Hibbard & Vacca (1997) which contains UGC galaxies classified as peculiar or interacting. We imposed the same size and surface brightness criteria while excluding galaxies already imaged by John Hibbard and collaborators. Lastly, for comparison we included 13 earlier type galaxies ( $T < 7$ ) and 24 unclassified or peculiar galaxies that were observed for other projects. The total sample therefore contains 142 galaxies, most of which are irregular or peculiar/merging.

Fig. 1 shows the resulting Hubble type distribution of our galaxy sample. It shows both the distribution of types from the RC3 and from our own visual classifications, which are the average of the values assigned to each galaxy by three different observers (V.A.T., S.C.O., S.H.C.)<sup>2</sup> experienced with classifying galaxies. A type of  $T=-9$  was assigned to the rare cases where no classification could be determined. Because mergers may play an important role in galaxy evolution via hierarchical galaxy formation models, a type of  $T=14$  was assigned to those galaxies that appeared to be interacting, or in the stages of a merger or post-merger. This extra class was created so that galaxies under the special condition of interactions and mergers could be treated separately. The bottom panel of Fig. 1 compares our classifications to those of the RC3, which for the most part agree. Differences between our classifications and those of the RC3 are partially due to galaxies that were unclassified in the RC3 being classifiable from our CCD images. Additionally, our classifiers classified several RC3 irregular types as late-type spirals. This misclassification in the RC3 is also

<sup>1</sup> RC3 total  $B$ -band magnitude per unit area within the RC3 25 mag arcsec<sup>-2</sup>  $B$ -band isophote.

<sup>2</sup> Violet A. Taylor, Stephen C. Odewahn, and Seth H. Cohen; Arizona State University

evident in the *HST* images of Windhorst et al. (2002), and is due to the difficulty of accurately classifying these small, faint galaxies with the photographic plates used for the RC3. These plates had lower spatial resolution, signal-to-noise, and dynamic range than our VATT CCD and *HST* images, such that faint spiral structure may have been missed.

Since most of our sample was chosen from the RC3, biases that are inherent in the RC3 itself will also exist in our own sample. We can test for the consistency of our sample with respect to the RC3 through a comparison between the samples of several quantities. Fig. 2 compares the (a) 25 mag arcsec<sup>-2</sup> *B*-band isophotal diameter, (b) axis ratio (*b/a*), (c) total *B*-band magnitude ( $B_T$ ), and (d) total (*B-V*) color distributions of the RC3 to the measurements for our sample. Only galaxies with diameters less than the  $\sim 6'$  FOV of the VATT CCD are included in Fig. 2a. This does not affect the shape of the distribution, since only  $\lesssim 1\%$  of the galaxies in the RC3 have diameters larger than  $6'$ . Our diameter distribution closely resembles that of the RC3. Fig. 2b shows that our sample is underrepresented in very flat galaxies, which is to be expected from the deficit of early- to mid-type spiral galaxies in our sample, which are more likely to appear flat when viewed edge-on. Our sample also peaks at a slightly fainter  $B_T$  magnitude and a much bluer ( $B-V$ ) $_T$  color than the RC3 (Fig. 2c and 2d, respectively). This is also to be expected with a late-type galaxy-selected sample, because later-type galaxies are on average fainter and bluer than earlier-type galaxies.

The six galaxies observed with *HST* NICMOS are part of a larger sample of 136 galaxies observed in the mid-UV (F300W) and near-IR (F814W) by WFPC2 (Windhorst et al. 2002; Eskridge et al. 2003; de Grijs et al. 2003), which overlaps significantly with our VATT sample. The entire *HST* data-set will be analyzed in more detail in later papers (e.g., Taylor et al. 2005, in prep.). The *HST* sample was chosen to include galaxies that were predicted to be UV bright and small enough for most of the galaxy to fit within the WFPC2 FOV.

## 2.2. Observations

We obtained our ground-based observations at the VATT at Mt. Graham International Observatory (MGIO, AZ) with the 2k $\times$ 2k Direct Imager because of its high sensitivity in the near-UV, which is critical for our ultimate science goals. The effective quantum efficiency in *U* is  $\sim 40\%$ , which includes transmission loss through the atmosphere combined with the  $\sim 75\%$  transmission of the CCD and the  $\sim 67\%$  transmission of the filter.<sup>3</sup> We binned the CCD images 2 $\times$ 2 upon read-out, giving a pixel scale of  $\sim 0''.375$  pixel<sup>-1</sup>. The typical seeing at the VATT is well sampled by this pixel scale (Taylor et al. 2004). The detector read-noise is  $5.7 e^-$  and the gain is  $1.9 e^-$  ADU<sup>-1</sup>. Typical exposure times used for the galaxies in our sample were 2 $\times$ 600 s in *U*, 2 $\times$ 300 s in *B*, 2 $\times$ 240 s in *V*, and 2 $\times$ 180 s in *R* for galaxies with average total surface brightness brighter than  $\mu_B = 24.0$  mag arcsec<sup>-2</sup>, and twice these exposure times for lower surface brightness galaxies. The long exposure times in *U* and *B* relative to *V* and *R* were chosen to

<sup>3</sup> <http://clavius.as.arizona.edu/vo/R1024/vattinst.html>

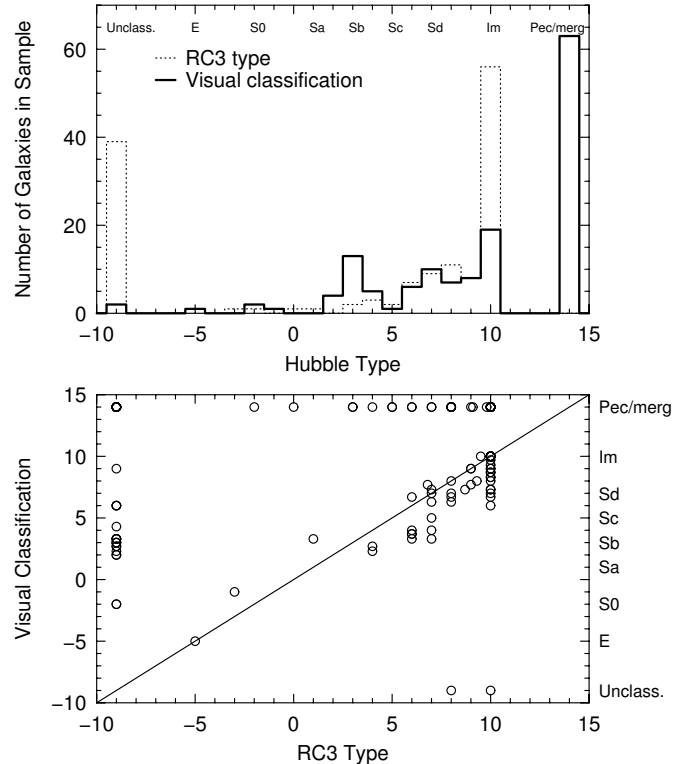


FIG. 1.— [Top panel] Distribution of morphological type in our sample of 142 galaxies, using classifications as listed in the RC3 (dotted) and as determined from our VATT *R*-filter images (solid). A numeric type  $T = -9$  indicates that no type was given in the RC3, or that it appeared unclassifiable by all of our classifiers. A type of  $T = 14$  indicates that our classifiers determined that the object was a strongly interacting galaxy pair, galaxies in the process of merging, or a likely merger remnant. Our sample concentrates on late-type, irregular, and peculiar/merging galaxies. [Bottom panel] Comparison of RC3 types to our visual classifications. Several RC3 irregular type galaxies were classified by our classifiers as late-type spirals, which may be due to faint spiral structure not being visible in the photographic plates used to classify these small, faint galaxies for the RC3.

overcome the lower sensitivity and higher atmospheric extinction in these pass-bands, such that colors within the galaxies can be reliably measured at larger radii before the low surface brightness *U* and *B* light is lost within the sky noise. Observations were spread over 9 runs between 1999 April and 2002 April. Photometric nights were defined as those with magnitudes measured for a particular standard star varying no more than 3% throughout the night. During photometric nights, short photometric exposures were taken of galaxies that were observed during non-photometric conditions.

Table 1 contains a list of all 142 galaxies for which we obtained a full set of calibrated observations in *UBVR*. The full table is available only in the electronic edition. Each galaxy is assigned an internal ID number (column 1), which we will use for brevity throughout the remainder of the paper when referring to a particular galaxy. The average sky background level in each image was determined by taking the median of the median pixel values in 13 120 $\times$ 120 pixel regions along the image border that were relatively devoid of objects. Thus, we minimize contamination by light from the galaxy, which is usually cen-

TABLE 1  
OBSERVED VATT GALAXY LIST.

ID# (1)	Galaxy (2)	RA (3)	DEC (4)	T <sub>RC3</sub> (5)	T (6)	Filter (7)	N <sub>exp</sub> (8)	T <sub>exp</sub> (9)	sec z (10)	Sky (11)	$\sigma_{\text{sky}}$ (12)	$\mu_{\text{sky}}$ (13)	Seeing (14)	$\sigma_{\text{seeing}}$ (15)	Obs. date (16)	Phot? (17)
001	UGC00156	00 <sup>h</sup> 16 <sup>m</sup> 46 <sup>s</sup> .30	+12°21′13″.1	10.0	9.3	U	2.0	1200.0	1.068	624.654	2.498	20.98	1.554	0.089	1999 Dec 07	n
...	...	...	...	...	...	B	2.0	600.0	1.073	971.057	3.935	21.67	1.470	0.115	1999 Dec 07	n
...	...	...	...	...	...	V	2.0	480.0	1.079	1666.022	13.948	20.65	1.403	0.044	1999 Dec 07	n
...	...	...	...	...	...	R	2.0	360.0	1.069	2230.095	17.548	20.00	1.963	0.153	1999 Dec 08	n
002	UGC00404	00 <sup>h</sup> 39 <sup>m</sup> 19 <sup>s</sup> .17	+13°06′40″.3	8.0	14.0	U	2.0	1200.0	1.108	654.128	5.195	20.99	1.965	0.119	1999 Dec 07	n
...	...	...	...	...	...	B	2.0	600.0	1.114	1024.339	18.580	21.53	1.680	0.163	1999 Dec 07	n
...	...	...	...	...	...	V	2.0	480.0	1.121	1762.469	18.790	20.73	1.374	0.103	1999 Dec 07	n
...	...	...	...	...	...	R	3.0	360.0	1.064	2195.478	41.374	20.06	2.021	0.186	1999 Dec 08	n
003	UGC00512	00 <sup>h</sup> 50 <sup>m</sup> 02 <sup>s</sup> .59	+07°54′55″.3	8.0	14.0	U	2.0	1200.0	1.342	740.667	4.676	20.78	1.845	0.077	1999 Dec 07	n
...	...	...	...	...	...	B	2.0	600.0	1.355	1211.626	6.261	21.15	1.813	0.056	1999 Dec 07	n
...	...	...	...	...	...	V	2.0	480.0	1.369	2221.780	23.531	20.54	1.691	0.045	1999 Dec 07	n
...	...	...	...	...	...	R	2.0	360.0	1.103	2380.214	16.848	19.94	1.926	0.133	1999 Dec 08	n
004	UGC00644	01 <sup>h</sup> 03 <sup>m</sup> 16 <sup>s</sup> .65	+14°02′01″.6	-9.0	14.0	U	2.0	600.0	1.436	328.397	2.273	20.88	1.905	0.175	1999 Dec 05	n
...	...	...	...	...	...	B	2.0	300.0	1.441	549.109	5.125	21.46	2.017	0.103	1999 Dec 05	n
...	...	...	...	...	...	V	2.0	240.0	1.446	961.138	13.536	20.56	1.742	0.047	1999 Dec 05	n
...	...	...	...	...	...	R	2.0	180.0	1.056	993.174	10.910	20.05	1.354	0.102	1999 Dec 06	n
005	UGC00749	01 <sup>h</sup> 11 <sup>m</sup> 30 <sup>s</sup> .28	+01°19′10″.9	8.0	14.0	U	2.0	600.0	1.186	313.720	1.674	20.98	2.239	0.215	1999 Dec 08	n
...	...	...	...	...	...	B	2.0	300.0	1.188	509.273	6.873	21.83	2.257	0.200	1999 Dec 08	n
...	...	...	...	...	...	V	2.0	240.0	1.190	901.062	11.823	20.61	2.130	0.176	1999 Dec 08	n
...	...	...	...	...	...	R	2.0	180.0	1.173	1032.213	17.354	19.89	1.266	0.153	1999 Dec 06	n
006	UGC00849	01 <sup>h</sup> 19 <sup>m</sup> 23 <sup>s</sup> .03	+12°26′57″.4	8.0	14.0	U	2.0	1200.0	1.173	555.018	3.437	21.16	2.398	0.625	1999 Dec 05	n
...	...	...	...	...	...	B	2.0	600.0	1.180	941.693	7.004	21.71	2.122	0.065	1999 Dec 05	n
...	...	...	...	...	...	V	2.0	480.0	1.189	1617.641	14.125	20.81	1.879	0.040	1999 Dec 05	n
...	...	...	...	...	...	R	2.0	360.0	1.075	1885.133	17.085	19.97	1.425	0.188	1999 Dec 06	n
007	UGC01104	01 <sup>h</sup> 32 <sup>m</sup> 43 <sup>s</sup> .47	+18°19′01″.4	10.0	10.0	U	2.0	600.0	1.080	321.698	1.520	20.20	1.860	0.167	2002 Jan 18	n
...	...	...	...	...	...	B	2.0	300.0	1.077	632.436	2.407	20.73	2.092	0.375	2002 Jan 18	n
...	...	...	...	...	...	V	2.0	240.0	1.077	1019.565	4.676	19.81	1.879	0.144	2002 Jan 18	n
...	...	...	...	...	...	R	2.0	180.0	1.076	1320.217	14.134	19.44	1.819	0.148	2002 Jan 18	n
008	UGC01133	01 <sup>h</sup> 35 <sup>m</sup> 00 <sup>s</sup> .85	+04°23′11″.8	10.0	14.0	U	2.0	1200.0	1.167	572.971	3.850	20.95	1.729	0.104	1999 Dec 04	n
...	...	...	...	...	...	B	2.0	600.0	1.174	941.990	8.528	21.59	1.729	0.154	1999 Dec 04	n
...	...	...	...	...	...	V	2.0	480.0	1.181	1618.724	14.945	20.76	1.521	0.201	1999 Dec 04	n
...	...	...	...	...	...	R	2.0	360.0	1.156	2233.333	25.213	19.42	1.118	0.048	1999 Dec 06	n
009	UGC01219	01 <sup>h</sup> 44 <sup>m</sup> 20 <sup>s</sup> .13	+17°28′42″.9	-9.0	3.0	U	2.0	600.0	1.068	184.311	0.804	21.27	1.447	0.169	2002 Jan 15	n
...	...	...	...	...	...	B	2.0	300.0	1.065	357.344	1.232	21.63	1.824	0.183	2002 Jan 15	n
...	...	...	...	...	...	V	2.0	240.0	1.064	542.139	1.726	20.94	1.744	0.276	2002 Jan 15	n
...	...	...	...	...	...	R	2.0	180.0	1.063	718.337	1.929	20.14	1.665	0.212	2002 Jan 15	n
010	UGC01240	01 <sup>h</sup> 46 <sup>m</sup> 19 <sup>s</sup> .56	+04°15′52″.5	8.0	14.0	U	2.0	600.0	1.273	290.342	2.543	21.11	1.991	0.117	1999 Dec 04	n
...	...	...	...	...	...	B	2.0	300.0	1.275	465.680	5.036	21.69	1.901	0.137	1999 Dec 04	n
...	...	...	...	...	...	V	2.0	240.0	1.278	823.495	8.784	20.75	2.070	0.041	1999 Dec 04	n
...	...	...	...	...	...	R	2.0	180.0	1.167	1215.579	14.472	18.73	1.211	0.076	1999 Dec 06	n

NOTE. — **Columns:** (1) ID number assigned to this galaxy, (2) galaxy name, (3) Right Ascension (J2000), (4) Declination (J2000), (5) RC3 classification, (6) visual classification, (7) filter, (8) number of images used in each stack, (9) average exposure time of those images (s), (10) average airmass (sec z), (11) median sky in ADU, (12) uncertainty on a single pixel measurement of the sky, (13) sky surface brightness in magarcsec<sup>-2</sup>, (14) average stellar FWHM ("seeing") (arcsec), (15) uncertainty on the seeing, (16) observation date of the first deep image combined into the final stack, and (17) whether the individual deep images were photometric: if no (n), then the deep images were calibrated with shorter photometric exposures. The full table is available only in the electronic edition.

tered within each image. Taking the median values also helps to reject stars, background galaxies, and cosmic rays. Sky gradients have little effect on these sky measurements since, after flat fielding, the sky background

in each image on scales of  $\sim 6'$  is flat to better than 1%, and typically to  $\sim 0.5\%$  in each of the filters. These sky-values were used in the reduction process, but local and global sky-values were recalculated in a more sophisti-

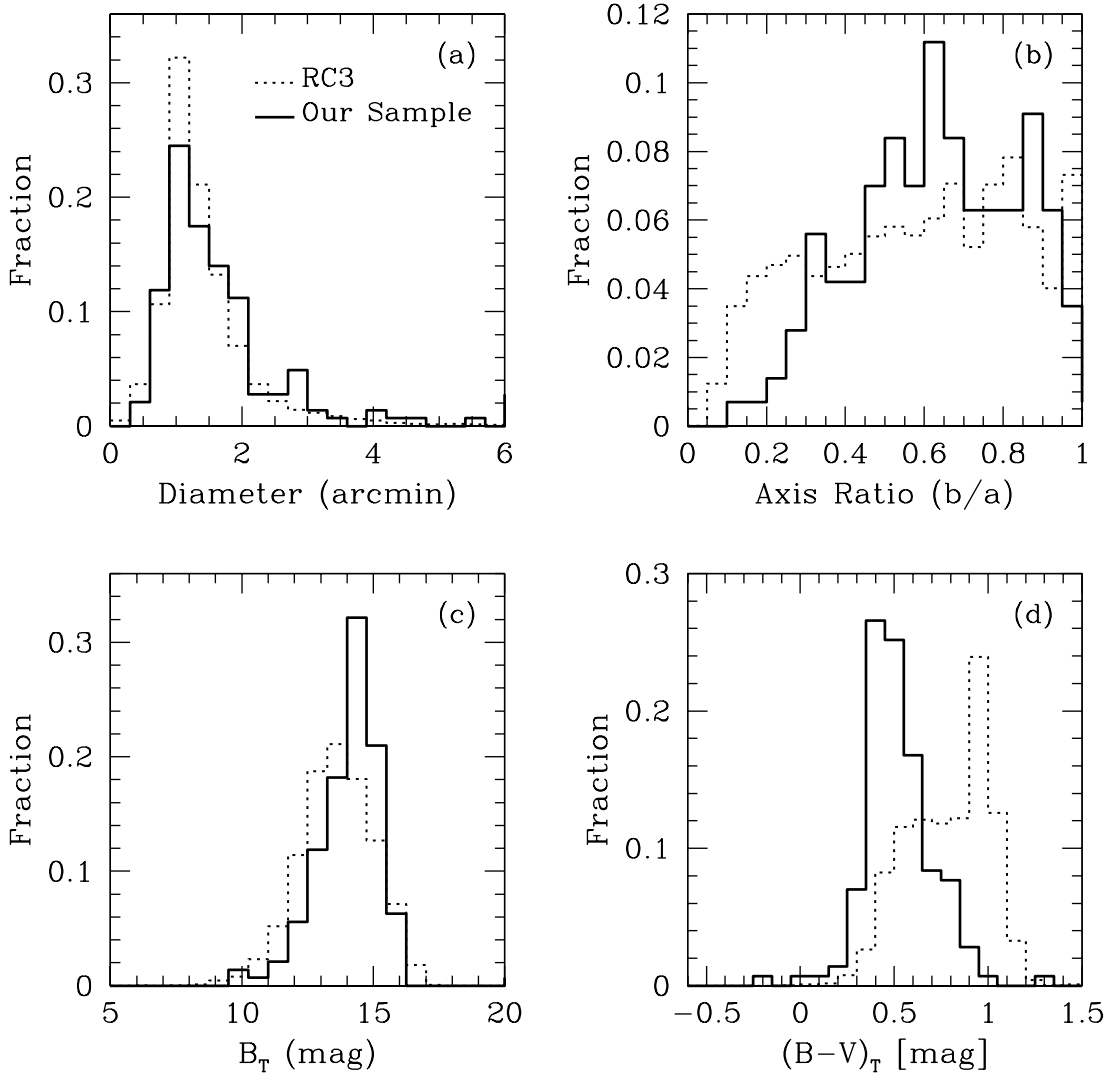


FIG. 2.— Distribution of the (a) 25 mag arcsec<sup>-2</sup>  $B$ -band isophotal diameter, (b) axis ratio ( $b/a$ ), (c) total  $B$ -band magnitude ( $B_T$ ), and (d) total  $(B - V)_T$  color of all galaxies in our sample (solid) compared to that in the RC3 (dotted). The diameter distribution of the galaxies in our sample is similar to that of the RC3. Our sample is underrepresented in very flat galaxies, which is expected from the selection effects of our particular sample, since late-type galaxies will not be as flat as earlier-type spiral galaxies when viewed edge-on. Our sample peaks at a slightly fainter  $B_T$  magnitude than the RC3, which is dominated by more luminous early-type galaxies. The bluer  $(B - V)$  color in our sample is the direct result of our selection of UV-bright, late-type galaxies.

cated way where appropriate, as described in sections below. Table 1 lists these sky background levels (column 11) and corresponding sky surface brightnesses (column 13) and seeing estimates (column 14) determined from the median stellar FWHM (full width at half maximum) in each image, using the method described in Taylor et al. (2004), where the sky surface brightness and seeing trends in these VATT data are analyzed in more detail.

The near-IR *HST* NICMOS  $H$ -band data, summarized in Table 2, were taken as part of Cycle 12 SNAP-shot program #9824 (P.I.: R. Windhorst), using NIC3 in the near-IR (F160W,  $\lambda_c = 15,500\text{\AA}$ , or  $1.55\ \mu\text{m}$ ). Three 500 s exposures were taken of each galaxy. Since NIC3 has a small FOV of  $51.2''$ , we dithered by about 45 pixels between the three observations to include more

of the galaxy in the final mosaic and to facilitate bad pixel removal. The NIC3 detector has a pixel scale of  $\sim 0''.20\ \text{pixel}^{-1}$ . The *HST*/WFPC2 mid-UV (F300W,  $\lambda_c = 2992\text{\AA}$ ) and  $I$  (F814W,  $\lambda_c = 8002\text{\AA}$ ) data (see Table 2) were taken as part of Cycle 9 GO program #8645 (Windhorst et al. 2002) or Cycle 10 SNAP-shot program #9124 (P.I.: R. Windhorst; Jansen et al. 2005, in prep.). We combined the two separate exposures per filter and the images of all four WFPC2 cameras into a single mosaic. Individual exposures in the mid-UV F300W filter were typically 300–1000 s, while we exposed 40–130 s in  $I$ . For the Cycle 9 data, the two individual exposures per filter were dithered by  $\sim 4$  pixels to facilitate rejection of bad pixels. The pixel scale in the combined WFPC2 images is  $\sim 0''.0996\ \text{pixel}^{-1}$ .

TABLE 2  
*HST* NICMOS AND WFPC2 DATASET.

galaxy	RA	DEC	T <sub>RC3</sub>	$r_{outer}$	$\delta_1$	$\sigma_{\delta_1}$	$\delta_2$	$\sigma_{\delta_2}$	$\delta_3$	$\sigma_{\delta_3}$
NGC1311	03 <sup>h</sup> 20 <sup>m</sup> 06 <sup>s</sup> .66	-52°11′12″.5	9.0	39.44	0.97	0.05	1.42	0.04	0.64	0.03
ESO418-G008	03 <sup>h</sup> 31 <sup>m</sup> 30 <sup>s</sup> .58	-30°12′46″.6	8.0	22.94	-1.05	0.04	-1.26	0.03	-0.26	0.03
NGC1679	04 <sup>h</sup> 49 <sup>m</sup> 55 <sup>s</sup> .31	-31°58′05″.5	9.5	33.61	-0.50	0.03	-0.85	0.03	-0.25	0.02
NGC2551	08 <sup>h</sup> 24 <sup>m</sup> 50 <sup>s</sup> .16	+73°24′43″.0	0.2	28.56	-2.39	0.03	-2.88	0.03	-0.50	0.01
NGC3516	11 <sup>h</sup> 06 <sup>m</sup> 47 <sup>s</sup> .48	+72°34′06″.7	-2.0	25.22	-0.35	0.06	-0.60	0.06	-0.25	0.02
NGC6789	19 <sup>h</sup> 16 <sup>m</sup> 41 <sup>s</sup> .93	+63°58′20″.8	10.0	23.51	2.09	0.08	1.87	0.07	-0.32	0.03

NOTE. — The six galaxies for which we have *HST* NICMOS F160W and WFPC2 F300W and F814W images. **Columns:** Galaxy name, Right Ascension (J2000), Declination (J2000), RC3 classification, the outer annulus radius used in the surface brightness profiles ( $r_{outer}$ ) in arcseconds, and the three color profile slopes and their errors (from the linear-least-squares fit) in units of  $\Delta\text{mag}$  per  $r_{outer}$ , where  $\delta_1$  is the slope in (F300W–F814W),  $\delta_2$  is the slope in (F300W–F160W), and  $\delta_3$  is the slope in (F814W–F160W).

### 2.3. VATT Data Reduction and Calibration

The median dark signal (column 2) and dark rates (column 4) measured in six dark images taken in April 2001 are listed in Table 3. Because these exposures were taken during the day when some sunlight may have leaked onto the detector, they represent an upper limit of the actual dark current, which may be even smaller. There is an average dark current of  $7.54 \pm 0.21$  ADU/hr, which results in a worst case scenario (column 5) of  $2.51 \pm 0.07$  ADU in our longest exposure of 1200 seconds in the *U*-band, and which is very small compared to the median *U* sky of  $492 \pm 12$  ADU. If dark current is neglected, this leads to a possible average error in the absolute sky determinations of 0.51% in *U*, 0.16% in *B*, 0.08% in *V*, and 0.05% in *R* (which only matters when finding the absolute sky surface brightnesses, and will not affect the galaxy photometry, even to second order). Much larger errors can be introduced through various other uncertainties in the photometry, and subtracting a dark image will only introduce another source of noise without any benefit to the large-scale galaxy surface photometry. Therefore, we did not subtract a dark image or a, likely overestimated, constant dark level from the images.

All images were zero subtracted, flat fielded, and calibrated with Landolt standard stars (Landolt 1992) using standard methods in IRAF.<sup>4</sup> The photometric zero-point for all images is accurate to within  $\sim 3\%$ . The VATT, at present, does not offer a reliable way of taking dome flats, so only twilight sky-flat fields were used. We were usually able to obtain at least 3–4 good evening sky-flats per filter per night, and at least another 3–4 morning sky-flats, which sufficed to remove all traces of high frequency structure. After flat-fielding, at most a 1% gradient in the sky background remained across the entire image. Differences in illumination of the detector between the twilight and night sky, which depend at least in part on the position of the telescope relative to the Sun and Moon, appear to be the cause. Because this gradient is less than 1% across the entire image, and because most of our galaxies are  $\sim 1'$  in size and centered in the exposure, galaxy photometry will be only slightly

<sup>4</sup> IRAF is distributed by the National Optical Astronomy Observatories, which are operated by the Association of Universities for Research in Astronomy, Inc., under cooperative agreement with the National Science Foundation.

TABLE 3  
 DARK CURRENT MEASUREMENTS.

T <sub>exp</sub>	⟨Dark⟩	$\sigma_{dark}$	hr <sup>-1</sup>	(1200s) <sup>-1</sup>
240	0.546	3.36	8.18	2.73
240	0.525	3.40	7.87	2.62
300	0.611	3.54	7.34	2.45
300	0.624	3.42	7.49	2.50
600	1.131	3.83	6.79	2.26
600	1.261	4.08	7.57	2.52

NOTE. — **Columns:** Exposure time (s) of the dark image, total median dark current (ADU) in the image, standard deviation on the median dark current, dark current rate (ADU hr<sup>-1</sup>), and the dark current (ADU 1200s<sup>-1</sup>) corresponding to our longest object exposures of 1200 s taken in the *U*-band. Most exposures are much shorter, down to 180 seconds. It was determined that this dark current is negligible and unnecessary to subtract from object images.

affected by this gradient, especially when compared to other larger sources of uncertainty. A 1% error in the sky corresponds on average to 27.0, 27.5, 26.5, and 26.0 mag arcsec<sup>-2</sup> in *U*, *B*, *V*, and *R*, respectively (as calculated from the average sky brightnesses presented in Taylor et al. (2004)), which is fainter than the level at which our surface brightness profiles are reliably determined, and therefore should have little effect on our results. Therefore, sky-gradient corrections were not applied.

Individual galaxy images were combined on a per filter basis with integer pixel shifts. This is sufficient for our purposes because the seeing is oversampled (with 4 to 5 pixels per FWHM, on average), and because this analysis focuses on large scale radial trends. We also normalized the images to an exposure time of 1 second, airmass of 1, and zero-point of 25 mag arcsec<sup>-2</sup>, for convenience. To verify the consistency of our photometry, we present a plot of the difference between our measured total *B*-band magnitudes and those from the RC3 vs. our measured total *B*-band magnitudes in Fig. 3. Our values agree with those of the RC3 within an average of 0.2 magnitudes, which is comparable to the total magnitude errors quoted in the RC3. There is no significant

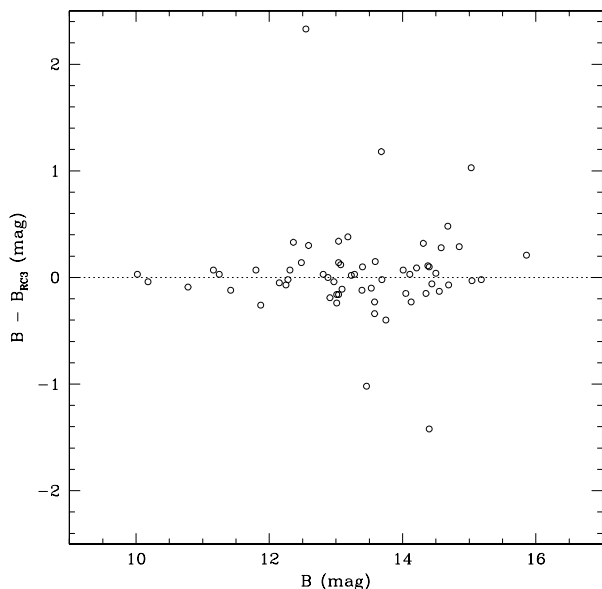


FIG. 3.— Comparison of our calibrated total  $B$ -band magnitudes to those listed in the RC3, for verifying the consistency of our photometry. Our measured magnitudes tend to agree with those of the RC3 within an average of about 0.2 magnitudes, which is generally comparable to the total magnitude errors quoted in the RC3. There is no significant systematic trend with  $B$ -band magnitude, which shows that our photometry is consistently accurate for all galaxy brightnesses.

systematic trend with total  $B$ -band magnitude, which shows that our photometry is consistently accurate for the full range of galaxy brightnesses.

Cosmic rays were removed using an IRAF script by Rhoads (2000), which rejects cosmic rays based on filtering out the point spread function (PSF) minus a user-scaled delta function, and rejecting any objects below a defined threshold to remove those objects that are much sharper than the PSF, and therefore cannot be real objects. The input parameters were modified by hand on a galaxy-per-galaxy basis to avoid erroneously rejecting pieces of the target galaxy. Any remaining cosmic rays were masked manually and interpolated over.

The images were astrometrically calibrated using LMORPHO (Odewahn et al. 2002), which calculates approximate astrometric solutions from user-interactive comparisons of several stars in the target image to the same stars in a DSS<sup>5</sup> image of the same region. It then refines the solutions by comparing all objects found with SExtractor (Bertin & Arnouts 1996) in the target image to accurate positions for all objects in this region listed in the USNO A2.0 catalog (Monet et al. 1996).

In order to obtain matched aperture photometry so that galaxy properties in different pass-bands can be directly compared to one another, the images in each filter were all registered with LMORPHO to the  $V$ -band,

<sup>5</sup> The Digitized Sky Surveys were produced at the Space Telescope Science Institute under U.S. Government grant NAG W-2166. The images of these surveys are based on photographic data obtained using the Oschin Schmidt Telescope on Palomar Mountain and the UK Schmidt Telescope. The plates were processed into the present compressed digital form with the permission of these institutions.

which was chosen as the reference pass-band because it typically has high signal-to-noise and few saturated stars. The SExtractor object lists were compared between filters to find linear shifts, and the images were shifted accordingly.

Finally, non-target objects were replaced with a local sky value ("patched") using LMORPHO, which uses positions from the object list created by SExtractor, and a user defined threshold value to patch out a large enough area to remove most of the light from each unrelated neighboring object. Each image was reviewed interactively to remove the target galaxy from the patch list, and to add any objects that SExtractor missed. In the case of interacting galaxies, the target was treated separately and the companion galaxy patched out unless there was no clear way to distinguish the galaxies, in which case they were treated as one. The patched area was replaced with an average value for the local sky that LMORPHO determined through an iterative sky-mapping procedure, which rejects objects above a certain signal-to-noise threshold level.

#### 2.4. HST Data Reduction and Calibration

Combined images of the *HST* WFPC2 mid-UV F300W and near-IR F814W observations were obtained as type B associations from the Space Telescope Science Institute (STSCI) data archive.<sup>6</sup> The associations were then mosaiced using WMOSAIC within the STSDAS package in IRAF.

The individual *HST* NIC3 F160W images were combined with CALNIB within the STSDAS package in IRAF, using shifts found semi-automatically with IMCENTROID. We used the VEGA zero point of 21.901 mag arcsec<sup>-2</sup> for the NICMOS data, calculated from the calibration data presented on the NICMOS website at STSCI.<sup>7</sup> Some bad pixels that were not removed with the pipeline bad pixel mask were removed by hand.

The WFPC2 images were registered to the NICMOS images by manually finding the coordinates of stars in common between images in each field, and by using these in GEOMAP and GEOTRAN in IRAF to apply the proper transformations. Non-target sources in all images were patched within LMORPHO to an average local sky-value using the same method as with the VATT data. We adopted the Holtzmann et al. (1995) zero points for each WFPC2 image.

### 3. DATA ANALYSIS

#### 3.1. Surface Brightness Profiles

Surface brightness profiles were calculated with LMORPHO for each galaxy within 12 equally spaced elliptical annuli, starting from the galaxy center. Parameters such as galaxy center, annulus radius, axis ratio, and position angle were chosen to match the shape of the outer isophotes, and were fixed in the  $R$ -band for the VATT data, and the NICMOS F160W band for the *HST* data. These were then applied to all other pass-bands in order to achieve matched aperture photometry that

<sup>6</sup> <http://archive.stsci.edu/hst/wfpc2/index.html>

<sup>7</sup> [http://www.stsci.edu/hst/nicmos/performance/photometry/postnics\\_keywords.html](http://www.stsci.edu/hst/nicmos/performance/photometry/postnics_keywords.html)

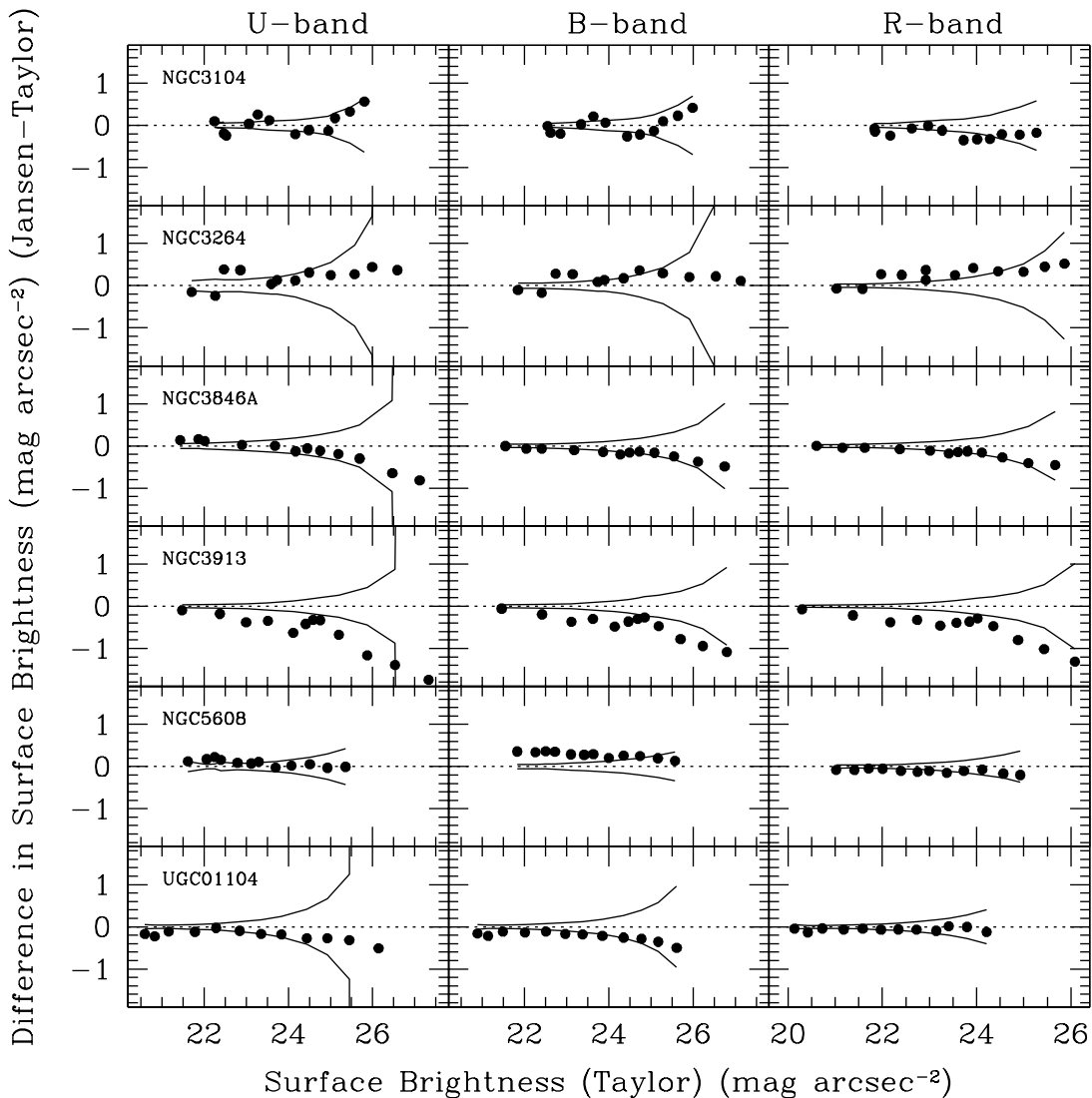


FIG. 4.— The difference in surface brightness ( $\Delta\mu$ ) at particular radii as a function of surface brightness  $\mu$  for 6 galaxies previously observed by Jansen et al. (2000). The difference is in the sense (Jansen et al. minus our profiles), and the abscissa reflects our measurements of  $\mu$ . As an aid in distinguishing significant differences, the solid curves indicate  $1\text{-}\sigma$  deviations, computed as the quadratic sum of the errors in the individual profiles. Deviations from zero in the inner parts of the galaxies result most frequently from a different choice of center, position angle and/or axis ratio, causing different morphological structures to be sampled. Deviations in the outer parts are dominated by sky-subtraction uncertainties. For the most part, both profiles agree to within the uncertainties – typically a few tenths of a magnitude. The galaxy showing the poorest agreement, NGC 3913, is asymmetric with significant spiral structure, causing differences in assumed shape and orientation to have a large impact. The position angles adopted here and in Jansen et al. differ by over  $50^\circ$ , which could account for the relatively large discrepancies.

could be directly and consistently translated into a color profile. The random error was calculated for the surface brightnesses with the formula:

$$\sigma = \sqrt{\frac{\sigma_{sky}^2}{N} + \frac{\langle F \rangle + \langle sky \rangle}{N}} \quad (1)$$

where  $\langle F \rangle$  is the measured average flux per pixel above sky within the annulus, and  $N$  is the number of pixels in the annulus. This does not include systematic errors due to small sky-subtraction errors, which can result in significant errors in the galaxy surface brightnesses as calculated at large radii, making the last few points in the surface brightness profiles less reliable than the inner points. Because the FOV in the VATT images ( $6.4'$ ) is much larger than the size of most of the galaxies (diam-

eter  $\sim 1'$ ), and because the fields tend to be un-crowded at high Galactic and Ecliptic latitude, we expect few objects to contaminate the VATT sky determinations. Errors due to the small ( $\lesssim 1\%$ ) gradients in the sky tend to drop out in the ellipse fitting, as long as the background shows no higher order structure. The *HST* NICMOS data, however, have a much smaller FOV ( $51.2''$ ). Therefore, it is much more difficult to obtain sky-values in the *HST* images that are not contaminated by the galaxy, and as such the points in the outer part of the *HST* profiles are less reliable than those in the VATT images. These larger uncertainties in the outer profile points are accounted for when determining color gradients, as described in § 3.2, such that they will have minimal impact on the accuracy of our final results.



Fig. 4 shows a comparison of our VATT surface brightness profiles in  $UBR$  to those of Jansen et al. (2000), for the 6 galaxies in common between our samples. For this comparison, our major axis radii,  $r$ , were converted to *elliptical* or *equivalent* radii,  $r_{ell} = r\sqrt{b/a}$ . The solid curves represent an estimate of the average  $1-\sigma$  error found by adding our errors in quadrature with those of Jansen et al. (2000). For the most part, both our profiles agree within the uncertainties, with a few slightly deviant points that can be attributed to various differences in the way that the two profiles were created. Jansen et al. (2000) applied a color term correction to each annulus separately, while we applied a single color term to the entire galaxy, based on its overall average color. The color term correction is small and difficult to measure accurately without a large number of standard stars of all colors taken throughout each observing night (which would sacrifice significant galaxy observing time). Therefore, errors introduced by using the average color of a galaxy to determine an average color term will be small compared to the errors inherent in measuring the small color term correction, and will therefore have little effect on our results. In extreme cases, this will cause the profiles to vary only slightly, if the galaxy color is a significant function of radius. Larger deviations in color gradient measurements are introduced by different choices of the galaxy center, and its axis ratio and position angle, which is especially an issue for galaxies with irregular or peculiar morphologies. For these morphologies, the choice of center is somewhat subjective, and the brightest peak often does not coincide with the center of the outer parts or disk. That center, and the shape and orientation of the isophotes, can vary significantly with radius. This effect can lead to vast differences in the choice of axis ratio and position angle, depending on how the observer chose to define them. In our case, these parameters were calculated automatically by LMORPHO, then inspected manually, with a few values tweaked to change the center, ellipticities, and position angles from the brightest un-centered peak to the center and shape of the outer disk. The choice of these parameters has the largest effect on the inner parts of the profiles, where a change in adopted axis ratio and orientation may result in different structures within the galaxy being sampled. The outer parts of the profile will be more dominated by sky subtraction errors. No attempt was made to correct for choice of the galaxy center, axis ratio, or position angle for this comparison.

Our profiles generally agree with those of Jansen et al. (2000) within a few tenths of a magnitude, which is similar to the differences they found in comparing their profiles with several other independent observers. The galaxy with the largest disagreement between our and Jansen et al.'s profiles is NGC3913, which is an asymmetric spiral galaxy. This asymmetry makes the choice of position angle and axis ratio particularly important, such that small changes in either could have a significant effect on the surface brightness profile. Here, Jansen et al. (2000) used an axis ratio ( $b/a$ ) of 0.9333 and a position angle (PA) (East of North) of  $165^\circ$ , compared to our  $b/a$  of 0.967 and PA of  $38.4^\circ$ , which could account for the relatively large discrepancy in our surface brightness profiles.

### 3.2. Color Profiles and Radial Color Gradients

Radial color profiles were calculated from the surface brightness profiles. The errors on the color profiles were calculated by adding the independent errors of the surface brightness profiles for each of the two filters (see Eq.[1]), converted to units of  $\text{mag arcsec}^{-2}$ , in quadrature. Using units of  $\text{mag arcsec}^{-2}$  is adequate, since the error on the flux,  $\sigma$ , will be small, and the error on the magnitude,  $\sigma_\mu$ , is related to the error on the log of the flux,  $\sigma_{\log(f)}$  by:

$$\sigma_\mu = 2.5 \sigma_{\log(f)} = 1.0857 \frac{\sigma}{f} \approx \frac{\sigma}{f}. \quad (2)$$

To measure the extent to which the VATT color profiles are becoming redder or bluer with increasing radius (color "gradient", or "slope"), we applied a linear-least-squares fit to the color profiles outside of the half-light, or *effective*, radius,  $r_e$  (as calculated from the  $R$ -band surface brightness profile), for the outer disk components, and separately applied a fit inside of  $r_e$  for the inner parts, which may be more affected by a bulge component, if present. Points where the measured average flux per pixel was smaller than  $0.5 \sigma_{sky}$  were not included in the fit in order to ignore values that have large uncertainties due to low signal-to-noise. To obtain more reliable color gradients, we weighted the points on the color profile by their errors. All radii were normalized to the effective radius in order to allow comparison of galaxies with various sizes. Therefore, our adopted units for the color profile slopes are the change in color ( $\Delta\text{mag}$ ) per unit effective radius ( $r_e$ ), where a positive slope indicates that a galaxy is getting redder with increasing radius from its center, and a negative slope indicates that it becomes bluer outward. If there were fewer than three good points in the inner or outer region of a galaxy, no slope was calculated for that region. Table 4 lists the outer color slopes (gradients) measured for all 142 galaxies (columns 16–19), as well as some other measured quantities such as effective radius (in both angular (column 3) and linear (column 4) units), total apparent and absolute  $B$  magnitudes (columns 7 and 8), average  $B$  surface brightness within  $r_e$  (column 12), and total (columns 9–11) and effective  $U-B$ ,  $B-V$ , and  $V-R$  colors (columns 13–15), where the effective color is defined as the average color within  $r_e$ . The entire table for all of the galaxies is provided only in the electronic version. Fig. 5a–5k show the first few VATT surface brightness and color profiles with their fits. The rest of the profiles (Fig. 5l–5el) are shown only in the electronic edition.

Due to the small FOV of the  $HST$  images and the low signal-to-noise at low surface brightness levels, the outermost parts of the galaxies are not necessarily detectable in the  $HST$  images, and it is thus not feasible to measure  $r_e$  from their surface brightness profiles. Therefore, we measured all  $HST$  color gradients across the entire galaxy profile, such that the units for the slopes are change in color ( $\Delta\text{mag}$ ) per  $r_{outer}$ , where  $r_{outer}$  is the radius of the outermost annulus used in the surface brightness profile (which was defined to go out far enough to include most of the light visible in the F160W image). When the signal-to-noise ratio was too low to reliably determine a surface brightness in an annulus, a surface brightness was not calculated for that annulus and not included in

TABLE 4  
VATT MEASURED GALAXY PARAMETERS.

ID# (1)	$D_{24}$ (2)	$r_e$ (") (3)	$r_e$ (kpc) (4)	b/a (5)	$V_{GSR}$ (6)	$B_T$ (7)	$B_T(abs)$ (8)	$(U-B)_T$ (9)	$(B-V)_T$ (10)	$(V-R)_T$ (11)	$\mu_e(B)$ (12)	$(U-B)_e$ (13)	$(B-V)_e$ (14)	$(V-R)_e$ (15)	$\delta(U-R)/r_e$ (16)	$\delta(U-B)/r_e$ (17)	$\delta(B-V)/r_e$ (18)	$\delta(V-R)/r_e$ (19)
001	95.61	26.88	2.33	0.540	1267.	14.580	-16.678	-0.083	0.576	0.394	23.150	-0.083	0.691	0.379	0.180	0.125	-0.112	0.157
...	...	...	...	...	...	0.024	0.064	0.037	0.032	0.029	0.027	0.043	0.037	0.034	0.159	0.171	0.118	0.105
002	51.13	14.90	10.93	0.460	10742.	15.836	-20.063	0.050	0.362	0.374	22.895	-0.179	0.405	0.374	0.251	0.364	-0.074	-0.048
...	...	...	...	...	...	0.041	0.071	0.064	0.057	0.055	0.047	0.072	0.066	0.066	0.251	0.266	0.202	0.189
003	45.74	10.60	3.98	0.770	5496.	14.966	-19.478	0.065	-0.004	0.640	21.986	0.065	0.185	0.636	-0.174	0.039	-0.476	0.323
...	...	...	...	...	...	0.024	0.064	0.038	0.036	0.034	0.031	0.047	0.048	0.048	0.084	0.088	0.105	0.100
004	58.99	10.85	...	0.420	...	15.382	...	0.063	0.662	0.652	21.836	0.158	0.760	0.780	0.395	0.079	-0.072	0.444
...	...	...	...	...	...	0.023	...	0.038	0.030	0.023	0.036	0.055	0.050	0.049	0.119	0.136	0.073	0.053
005	85.13	12.65	5.94	0.280	6882.	14.560	-20.372	-0.678	0.653	0.285	20.949	-0.790	0.765	0.441	-0.050	0.048	-0.035	-0.054
...	...	...	...	...	...	0.013	0.061	0.017	0.017	0.016	0.031	0.045	0.045	0.047	0.025	0.027	0.029	0.027
006	58.12	11.49	11.31	0.620	14410.	14.805	-21.732	-0.081	0.572	0.532	21.686	-0.072	0.677	0.532	-0.083	0.093	-0.109	-0.068
...	...	...	...	...	...	0.019	0.062	0.029	0.025	0.022	0.028	0.040	0.039	0.039	0.046	0.052	0.046	0.038
007	72.83	13.39	0.71	0.610	775.	14.507	-15.683	-0.153	0.533	0.448	21.393	-0.333	0.413	0.364	0.569	0.298	0.188	0.120
...	...	...	...	...	...	0.019	0.062	0.028	0.026	0.023	0.029	0.042	0.040	0.038	0.089	0.098	0.067	0.059
008	26.98	14.53	2.02	0.920	2031.	14.684	-17.598	-0.432	0.077	-1.138	22.973	-0.310	0.204	-0.690	...	-0.134	-0.202	...
...	...	...	...	...	...	0.081	0.100	0.113	0.126	0.233	0.051	0.070	0.082	0.256	...	0.660	0.697	...
009	81.79	10.43	3.35	0.530	4708.	13.718	-20.390	0.178	0.709	0.592	20.871	0.488	1.102	0.957	-0.157	-0.050	-0.063	-0.042
...	...	...	...	...	...	0.009	0.060	0.015	0.011	0.009	0.022	0.030	0.034	0.039	0.016	0.018	0.014	0.010
010	67.98	11.07	1.41	0.300	1862.	15.102	-16.992	-0.324	0.401	0.173	21.136	-0.203	0.401	0.301	-0.495	-0.262	-0.033	-0.205
...	...	...	...	...	...	0.019	0.062	0.026	0.026	0.032	0.037	0.051	0.053	0.059	0.203	0.170	0.163	0.198

NOTE. — **Columns:** (1) Galaxy ID number assigned in table 1, (2)  $R$ -band 24th magnitude isophotal diameter in arcseconds, (3)  $R$ -band effective radius within which half of the light is contained in arcseconds, (4)  $r_e$  in kpc using  $H_0 = 71 \text{ km s}^{-1} \text{ Mpc}^{-1}$ , (5) axis ratio, (6) RC3 Galactic standard of rest velocity in  $\text{km sec}^{-1}$ , (7) total  $B$ -band apparent magnitude derived from extrapolating the surface brightness profile to infinity, (8) total absolute  $B$ -band magnitude, average total colors for (9)  $(U-B)_T$ , (10)  $(B-V)_T$ , and (11)  $(V-R)_T$ , (12)  $B$ -band surface brightness within  $r_e$ , average colors within  $r_e$  for (13)  $(U-B)_e$ , (14)  $(B-V)_e$ , and (15)  $(V-R)_e$ , and color gradients outside of  $r_e$  (measured by finding the slope of the linear fit to the color profile for all good points outside of  $r_e$ ) in units of  $\Delta\text{mag}$  per  $r_e$  for (16)  $U-R$ , (17)  $U-B$ , (18)  $B-V$ , and (19)  $V-R$ . A negative slope indicates the galaxy becomes bluer with increasing radius, and a positive slope indicates that it gets redder outward. The second line for each galaxy lists errors for some quantities. The  $B_T$  error was derived from the total signal-to-noise in the largest aperture measured.  $B_T(abs)$  errors also include the uncertainty on  $H_0$  from WMAP measurements. Errors on the total and effective colors,  $(X-Y)_T$  and  $(X-Y)_e$ , are the quadratic sum of the respective total  $X$  and  $Y$  magnitude errors. The  $\mu_e(B)$  error is the accidental error derived from EQ. 1. The errors on the color gradients were determined from the scatter of the fits. *The full table is available only in the electronic edition.*

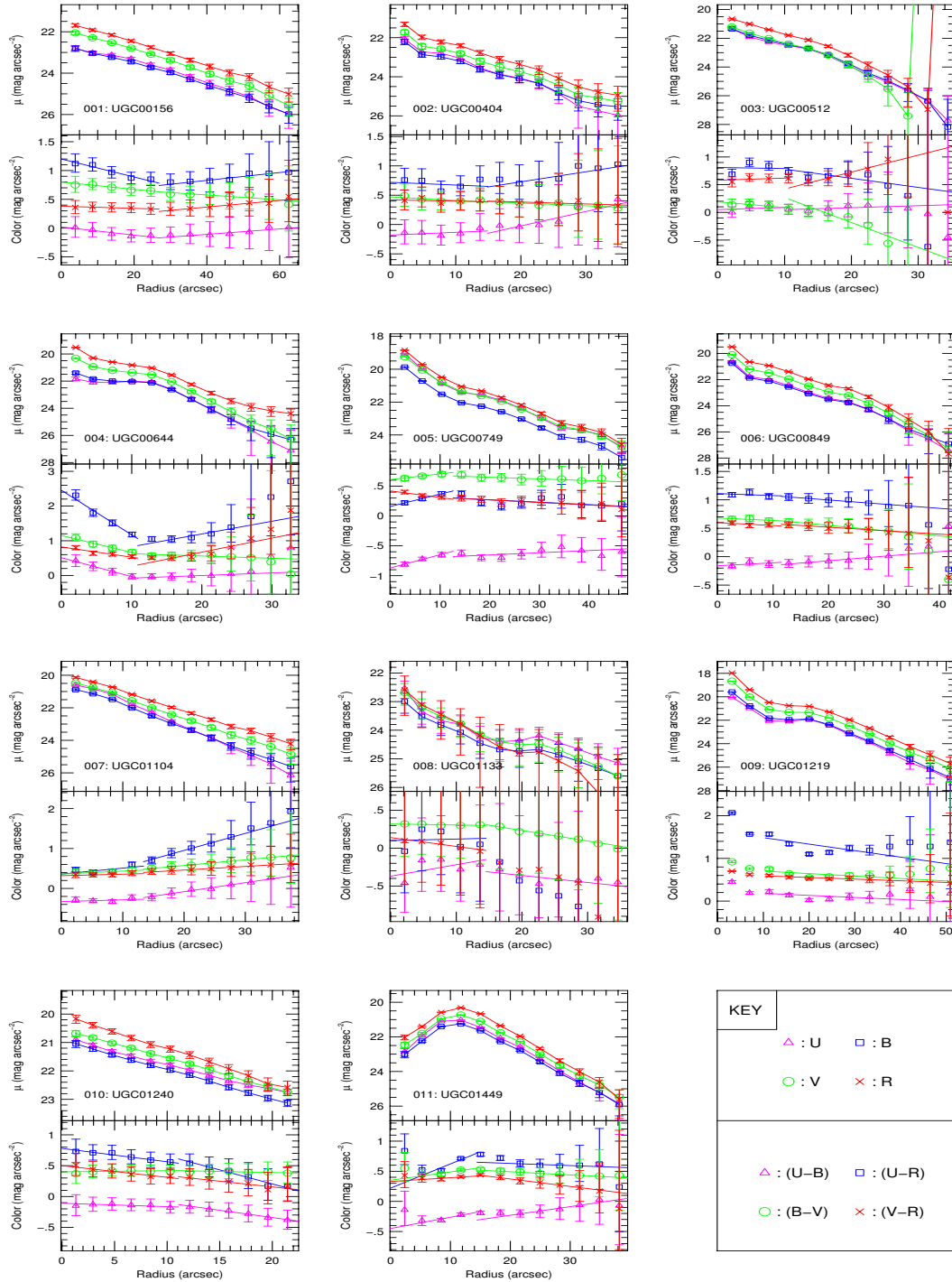


FIG. 5.— [Top panels] Surface Brightness ( $\mu$ ) profiles and [Bottom panels] color profiles for each of the 142 galaxies imaged at the VATT. The lines in the color profile plots are the error-weighted linear-least-squares fit to the data points inside  $r_e$  and outside  $r_e$ . No fit was made if there would be fewer than three good (signal-to-noise ratio above sky  $> 0.5$ ) points in the fit. *The remainder of the plots (Figs. 5l–5e) appear only in the electronic edition.*

the color slope calculation. The remaining points were weighted by their errors, except for the inner-most point of NGC3516, which was eliminated from the fit because the galaxy’s center is saturated in the WFPC2 images. The color gradients measured from the *HST* F300W, *I* and *H* surface brightness profiles are listed in Table 2.

#### 4. RESULTS

##### 4.1. VATT (*U*–*R*) Radial Color Gradients

Fig. 6 shows examples of the surface brightness and color profiles for a few VATT galaxies with notable radial color gradient trends, along with images of the galaxies in *U* and *R* with ellipses marking the outer annulus used to calculate the final point in the surface brightness profiles. NGC4476 is an early-type galaxy ( $T = -1.0$ ) with no significant radial color gradient, although it does become slightly bluer with radius. UGC04095 is a mid-type spiral ( $T = 6.0$ ) which becomes similarly slightly bluer with increasing radius. UGC01104 and UGC00156 are late-type galaxies ( $T = 10.0$  and  $9.3$ , respectively) that become redder with increasing radius. UGC01104 and UGC00156 differ in that UGC01104 gets redder with increasing radius throughout (in the inner parts ( $r < r_e$ ), and the outer parts ( $r > r_e$ )), while UGC00156 gets bluer with radius in the inner parts ( $r < r_e$ ) and redder in the outer parts ( $r > r_e$ ). This flip in color slope sign is common, occurring in about half of our galaxies.

The slopes of the outer “disk” ( $r > r_e$ ) *U*–*R* color profile fits measured in our VATT images are plotted vs. Hubble type, total absolute *B* magnitude,  $r_e$  in kpc (for  $H_0 = 71 \text{ km s}^{-1} \text{ Mpc}^{-1}$ ), and axis ratio ( $b/a$ ) in Fig. 7. The *U*–*R* color is shown because it provides the largest wavelength baseline, but the same trends are seen in all other possible *UBVR* color combinations. The color slope is zero if there is no change in color with radius, positive if the galaxy becomes redder at larger radii, and negative if the galaxy becomes bluer at larger radii. An error bar in the upper left panel shows the representative median uncertainty on the *U*–*R* color gradient slopes, as derived from the linear-least-squares fit. Median color slopes for several type bins are plotted as open triangles on top of the individual data points in the Hubble type plot. Boxes surrounding each median value enclose the type bin and the color slope 25% and 75% quartile ranges. Vertical error bars on these points indicate the error on the median ( $T_{50}$ ), which is calculated from the 25% ( $T_{25}$ ) and 75% ( $T_{75}$ ) quartile values with:

$$\sigma_{T_{50}} = \frac{1.483(T_{75} - T_{25})}{2\sqrt{N} - 1} \quad (3)$$

The median color slope becomes larger (redder with increasing radius), and the overall scatter, or range of possible color slopes, increases with later Hubble types, less luminous total magnitudes, smaller effective radii, and, to a lesser extent, rounder axis ratios. This similarity in trends is not surprising, since all of these parameters are not entirely independent, with later Hubble type galaxies tending to be fainter, smaller, and sometimes rounder than earlier type galaxies, with disks that are less rotationally supported.

The median color gradients in the plot of slope vs. Hubble type (Fig. 7) show that galaxies with types E

through S0 have no significant radial color slope within the  $1\text{-}\sigma$  error on the median ( $-0.02 \pm 0.03 \text{ mag arcsec}^{-2}$  per  $r_e$ ), or at most a very slight negative slope that would indicate a weak trend of bluer colors with increasing radius. Although this is determined from small number statistics (four galaxies), it is consistent with the findings from other studies of elliptical galaxy color gradients (Vader et al. 1988; Franx et al. 1989; Peletier et al. 1990). There is also no significant color gradient for early-type spirals (Sa-Sb), which at most get slightly redder with increasing radius ( $0.02 \pm 0.05 \text{ mag arcsec}^{-2}$  per  $r_e$ ). Mid-type spirals (Sc) tend to get bluer with increasing radius by  $1.8\text{-}\sigma$  ( $-0.11 \pm 0.06 \text{ mag arcsec}^{-2}$  per  $r_e$ ). This is also consistent with the findings in previous studies (de Jong 1996; Tully et al. 1996; Jansen et al. 2000; Bell & de Jong 2000; MacArthur et al. 2004). We see a significant (about  $3.6\text{-}\sigma$ ) trend of redder colors with increasing radius for most of the late-type spirals and irregulars, with a median color gradient of  $0.25 \pm 0.07 \text{ mag arcsec}^{-2}$  per  $r_e$  for late-type spirals and a gradient of  $0.27 \pm 0.07 \text{ mag arcsec}^{-2}$  per  $r_e$  for irregular galaxies. This suggests a distinction between the radial color gradient properties of elliptical and early to mid-type spiral galaxies (typically zero color gradients to a slightly bluer color with increasing radius, with some scatter between individual galaxies) vs. those of late-type spiral and irregular galaxies (typically redder color with increasing radius, with large scatter between individual galaxies). The peculiar and merger group ( $T = 14$ ) becomes on average slightly redder with increasing radius ( $0.07 \pm 0.03 \text{ mag arcsec}^{-2}$  per  $r_e$ ), although it has a large scatter in measured color gradients. This large scatter may be due to the particular physics of each galaxy interaction, since wide-spread massive star formation can be triggered anywhere in such galaxies and result in either positive or negative color gradients. Dust may also play a role in reddening the inner parts of these galaxies, which would further decrease the color gradient. These two factors are particularly pronounced in currently merging galaxies, and therefore may account for the more modest median color gradient we find for the interacting/merging group compared to the irregular galaxy group.

Fig. 8 contains plots of the *U*–*R* outer color slope vs. several other galaxy quantities derived from the RC3. Galaxies that did not have the relevant parameters listed in the RC3 were left out of the plot. The Hubble types from the RC3 show a similar trend with radial color gradient as our visual classifications (Fig. 7), with on average more galaxies becoming increasingly redder with increasing radius, and a larger gradient scatter with increasing Hubble type. This same trend is seen with increasing major axis diameter (which was converted to kpc using  $H_0 = 71 \text{ km s}^{-1} \text{ Mpc}^{-1}$ ), and with increasing radial velocity with respect to the Galactic standard of rest,  $V_{GSR}$ . The former is not surprising, since later-type galaxies tend to be intrinsically smaller than earlier-type galaxies. The trend with radial velocity is likely due to Malmquist Bias: since late-type galaxies tend to have a lower surface brightness than earlier-types, they will be preferentially selected at nearer distances when using surface brightness limited samples.

There is a weaker trend of increasingly redder outer re-

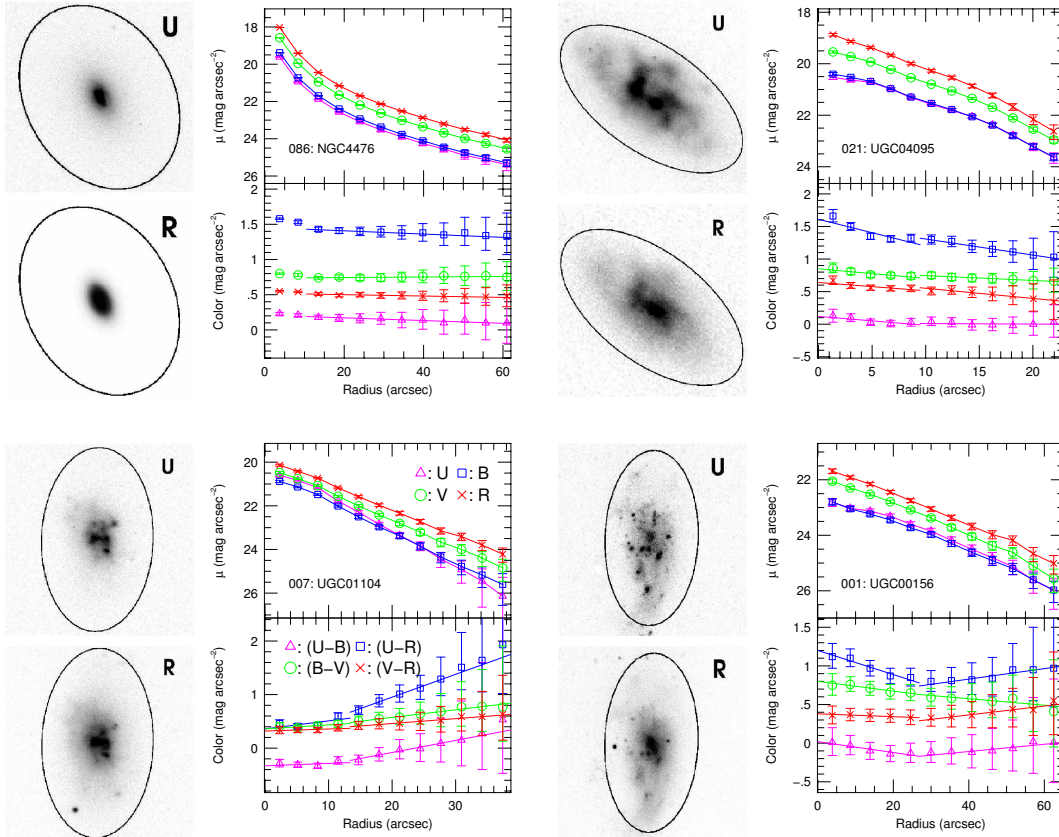


FIG. 6.— Examples of surface brightness and color profiles for some notable galaxies. The ellipses in the images mark the last annulus used in the profile calculation. Note that the images were scaled to highlight interesting galaxy structure, such that not all low-surface brightness structure may be visible in these images. The upper right panel for each galaxy is the surface brightness profile, and the lower right panel is the color profile, with the same color legend as in Fig. 5. The key printed in the UGC01104 plot applies to all of the plots. NGC4476 is an early-type ( $T = -1.0$ ) galaxy with constant to slightly bluer colors with increasing radius, which is typical of early-type galaxies. UGC04095 is a mid-type ( $T = 6$ ) spiral that also gets slightly bluer with radius, which is typical of mid-type galaxies. UGC01104 is an irregular galaxy ( $T = 10$ ) that gets redder with radius, which is more typical of late-type galaxies. UGC00156 is a late-type spiral galaxy ( $T = 9.3$ ) which actually gets bluer in the inner regions with radius, but redder in the outer regions. This change in color gradient sign is common, occurring in about half of the galaxies in our sample.

gions with fainter  $B_T^0$  (the absolute extinction corrected total  $B$ -band magnitude),  $M_{21}$  (the absolute H I 21 cm emission line magnitude), and, to a lesser extent,  $M_{FIR}$  (the absolute far infrared magnitude). This trend is also seen with mean  $B$ -band surface brightness,  $\mu_B$ , within  $r_e$ , although the low number statistics in this plot are due to the absence of effective radii ( $r_e$ ) information for many galaxies in the RC3. The H I index ( $(M_{21} - B_T^0)$  color) does not display a strong trend with color gradient, even though it is apparent in  $B_T^0$  and  $M_{21}$ . This suggests that galaxies that are overall intrinsically faint in all bands, which tends to be the case for late-type galaxies, have on average stronger gradients of redder colors with increasing radius, but that these are not necessarily caused by an excess of H I. This coupled with the very weak trend seen in  $M_{FIR}$ , suggests that the increasingly redder outer regions of late-type galaxies may not be due to excess dust, but perhaps to other factors such as stellar population gradients. This is in agreement with the conclusions of other authors, who find that the observed color gradients for mid- to late-type galaxies are most likely due to stellar population effects (Vader et al. 1988; de Jong 1996; Jansen et al. 2000; Bell & de Jong 2000;

MacArthur et al. 2004). It would be interesting to verify this with a thorough study of the spatial stellar population and dust content of late-type galaxies. There is no strong trend seen with  $\log(V_{max})$ , which is the log of the maximum rotational velocity in  $\text{km s}^{-1}$  of the galaxy, although this is based on low number statistics due to the absence of this information for most of the galaxies in the RC3. The four galaxies with the largest  $V_{max}$ , however, have small color gradient slopes, which is consistent with the most massive galaxies being earlier type galaxies, which have been shown in multiple studies to have small color gradients with bluer regions typically at larger radii (Vader et al. 1988; Franx et al. 1989; Peletier et al. 1990).

These results raise the question of whether the late-type galaxies that get redder with increasing radius actually have redder colors in their outskirts than other galaxies (perhaps due to a particularly old stellar population in the outer disk, or a radially increasing dust content), or whether they simply have uncommonly blue inner regions (perhaps due to younger or more metal poor stars in the inner parts of the galaxy). Fig. 9 addresses

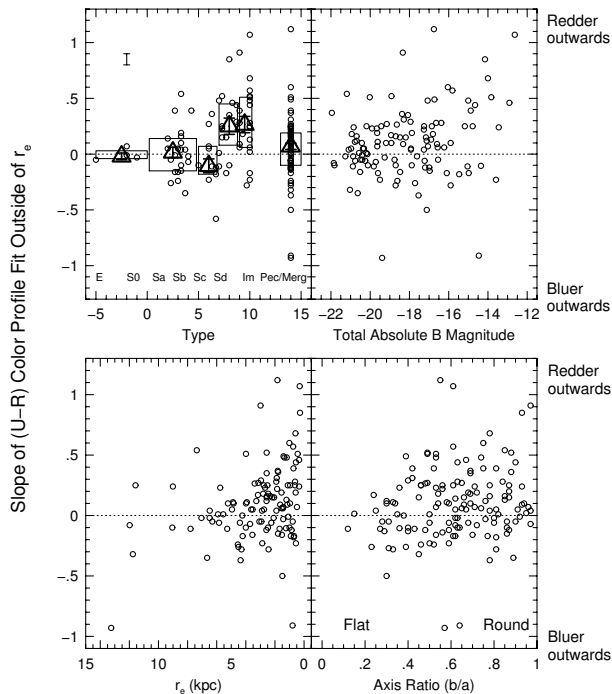


FIG. 7.— The  $U-R$  color gradient slope outside  $r_e$  (i.e., in the outer “disk”) plotted against several galaxy parameters. The error bar in the upper left corner of the type panel (upper left) shows the representative median error of the  $U-R$  color gradient slope. The triangles in this panel represent the median color slope for several type bins. Boxes surrounding each median value enclose the type bin and the color slope 25% and 75% quartile ranges. Vertical error bars mark the errors on the medians. There is no significant median color slope within the errors for early-type (E-S0) galaxies, or for early-type (Sa-Sb) spirals. Mid-type (Sc) spiral galaxies get slightly bluer with increasing radius, and late-type (Sd-Im) galaxies get significantly redder with increasing radius. Mergers/peculiarities get on average slightly redder with increasing radius, although they have a large range in color slope. The scatter in this panel increases with increasing Hubble type, such that there is a wider range of possible color slopes with increasing type. The other panels show an average trend of fainter, smaller, and rounder galaxies (which tend to have later Hubble types) becoming increasingly redder with radius, with an increasingly larger range of possible slope values (larger scatter).

this with a plot of the  $U-R$  color profile slope vs. the total integrated  $U-R$  color inside  $r_e$  (“bulge” color), and vs. extrapolated  $U-R$  color at  $2r_e$  (outer “disk” color). Different symbols represent different Hubble type bins. The early-type ( $T < 3$ ), mid-type ( $3 \leq T < 7$ ), and merger/interacting ( $T = 14$ ) galaxies do not show any significant trend in inner or outer color with color slope. Thus, the non-zero color gradients are not simply a mathematical artifact of these galaxies having an overall blue or red color, but are a meaningful measure of a radial gradient in other physical properties of these galaxies. Late Hubble type ( $7 \leq T \leq 10$ ) galaxies also show little trend in general, although as these galaxies get redder with increasing radius, they tend to be bluer in their inner regions, *as well as* redder in their outer regions than other galaxies. *This suggests that, for late-type galaxies, most of the galaxies that get redder with radius are actually bluer in their inner regions and redder in their outskirts than late-type galaxies that get bluer with radius.* If this is due to stellar population differences (which is the favored explanation of previous studies for

color gradients), and not dust or other possible factors, this could be an indicator that late-type galaxies that get redder with increasing radius form from the outside-in, with a relatively high amount of recent star formation in the inner regions (compared to other galaxies), and a relatively low amount of recent star formation in the outer regions.

#### 4.2. HST Radial Color Gradients

Fig. 10 shows all six *HST* surface brightness and color profiles with images of each galaxy in all three pass-bands. The ellipse on each image marks the outer annulus used for the last point in the profiles. NGC3516 is an early-type galaxy ( $T_{RC3} = -2.0$ ) that becomes slightly bluer with radius in each of the colors ( $F300W-F814W$ ), ( $F300W-F160W$ ), and ( $F814W-F160W$ ). NGC2551, which is also an early-type galaxy ( $T_{RC3} = 0.2$ ), gets significantly bluer with increasing radius in ( $F300W-F814W$ ) and ( $F300W-F160W$ ), but is fairly constant in color with radius in ( $F814W-F160W$ ) (or, at most, gets slightly bluer with radius). NGC1679 ( $T_{RC3} = 9.5$ ) and ESO418-G008 ( $T_{RC3} = 8.0$ ) are late-type galaxies that get slightly bluer with increasing radius in all colors, which is true for half of the late-type galaxies. Of the other two late-type galaxies, NGC6789 is an irregular galaxy ( $T_{RC3} = 10$ ) that gets significantly redder with increasing radius in ( $F300W-F814W$ ) and ( $F300W-F160W$ ), but gets slightly bluer with increasing radius in ( $F814W-F160W$ ). NGC1311 is a late-type magellanic spiral (Sm) galaxy ( $T_{RC3} = 9$ ) that gets redder with increasing radius in ( $F300W-F814W$ ) and ( $F300W-F160W$ ). It is the only one of these six galaxies that gets redder with increasing radius in ( $F814W-F160W$ ).

We plot the color slopes for the six *HST* galaxies vs. RC3 Hubble type in Fig. 11. Due to small-number statistics, broad conclusions cannot be confidently drawn from these results, but it is encouraging to note that the ( $F300W-F814W$ ) and ( $F300W-F160W$ ) color gradients show similar trends as those of  $U-R$  in the VATT data, with earlier galaxy types getting bluer with increasing radius, and later galaxy types becoming either bluer or redder with increasing radius. Five out of the six galaxies get slightly bluer with increasing radius in ( $F814W-F160W$ ). The magnitude of the ( $F814W-F160W$ ) color gradient does not depend on Hubble type, at least for these five galaxies. This may not be a surprising result since the F814W (8002 Å) and F160W (15,500 Å) filters don’t sample significantly different portions of galaxy spectra. The only outlier is NGC1311, which becomes significantly redder with increasing radius in ( $F814W-F160W$ ). Comparison of the NGC1311 images to the others reveal no inconsistencies in image quality that might cause this difference.

The F300W filter samples mid-UV light shortward of the atmospheric cut-off and the Balmer break, which contributes to color gradients that are sensitive to the presence of recent star formation. This may indicate that the redder outer parts of later Hubble type galaxies in ( $F300W-F814W$ ) may be primarily due to recent star formation concentrated near the center of these particular galaxy types. This young stellar population may exist amongst an underlying redder, older, population that

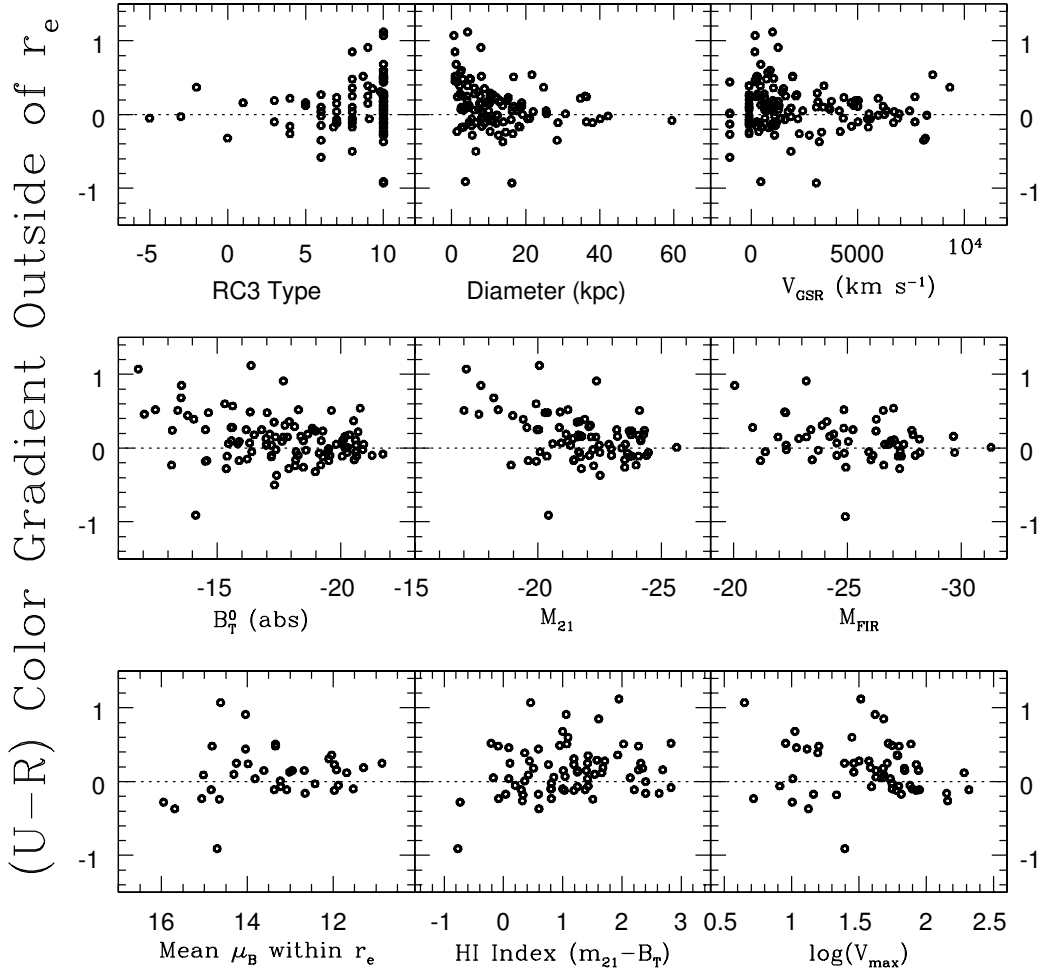


FIG. 8.— Radial  $U-R$  color gradient slope vs. (left to right, top to bottom): RC3 Hubble type, major axis diameter in kpc ( $H_0 = 71 \text{ km s}^{-1} \text{ Mpc}^{-1}$  for all calculations), radial velocity with respect to the Galactic standard of rest, extinction corrected total absolute  $B$ -magnitude, 21 cm emission line absolute magnitude, far infrared ( $60 - 100 \mu\text{m}$ ) absolute magnitude, mean  $B$  surface brightness within  $r_e$ , HI index  $= (M_{21} - B_T^0)$ , and the log of the maximum rotational velocity in  $\text{km s}^{-1}$ .

becomes more dominant toward the center of the galaxy, as evidenced by the bluer ( $F814W-F160W$ ) color with increasing radius for most of the galaxies. The degenerate possibilities of increasing metallicity or dust toward the center of the galaxy may also explain the ( $F814W-F160W$ ) gradients.

## 5. DISCUSSION

The bottom-up hierarchical structure formation model suggests that galaxies as they exist today were formed by the initial collapse of small mass fluctuations in the early Universe, and the subsequent merging of these small systems into larger ones (e.g., White 1979; White & Frenk 1991; Cole et al. 1994; Kauffmann et al. 1997; Roukema et al. 1997; Baugh et al. 1998). In this formation model, galaxy mergers and interactions would be common factors in galaxy evolution. Mergers and interactions have been shown to trigger starbursts (e.g., Mihos & Hernquist 1994, 1996; Hernquist & Mihos 1995; Barnes & Hernquist 1996; Somerville et al. 2001), which affect the radial color gradients of the galaxies. Starbursts can also be caused by bar instabilities (e.g., Noguchi 1988; Shlosman et al. 1989, 1990; Mihos & Hernquist 1994; Friedli

& Benz 1993, 1995) or triggered by superwind shocks created by a combination of supernovae and winds from massive stars (e.g., De Young 1978; Dekel & Silk 1986; Mathews 1989; Heckman et al. 1990), but at high redshift, galaxy mergers and interactions should be the most common cause. In this case, mergers and interactions would funnel gas to the central regions of the galaxy and trigger nuclear starbursts. In the simplest picture, this would result in galaxies that recently underwent a merger or strong interaction becoming redder outward (Moth & Elston 2002). Many gas-rich interacting galaxies, however, show significant star formation in their outer parts, where tidal disturbances can trigger star formation. Dust in the interiors of these galaxies may also redden their colors. Thus, given the complexities of galaxy interactions and the large range in properties of the galaxies involved in such interactions, some galaxies that recently underwent an interaction will become redder while others will become bluer with increasing radius—consistent with our results.

If this overall picture of galaxy assembly is correct, then galaxies that more recently underwent a hierarchical merger or accretion event would be *more likely* to become

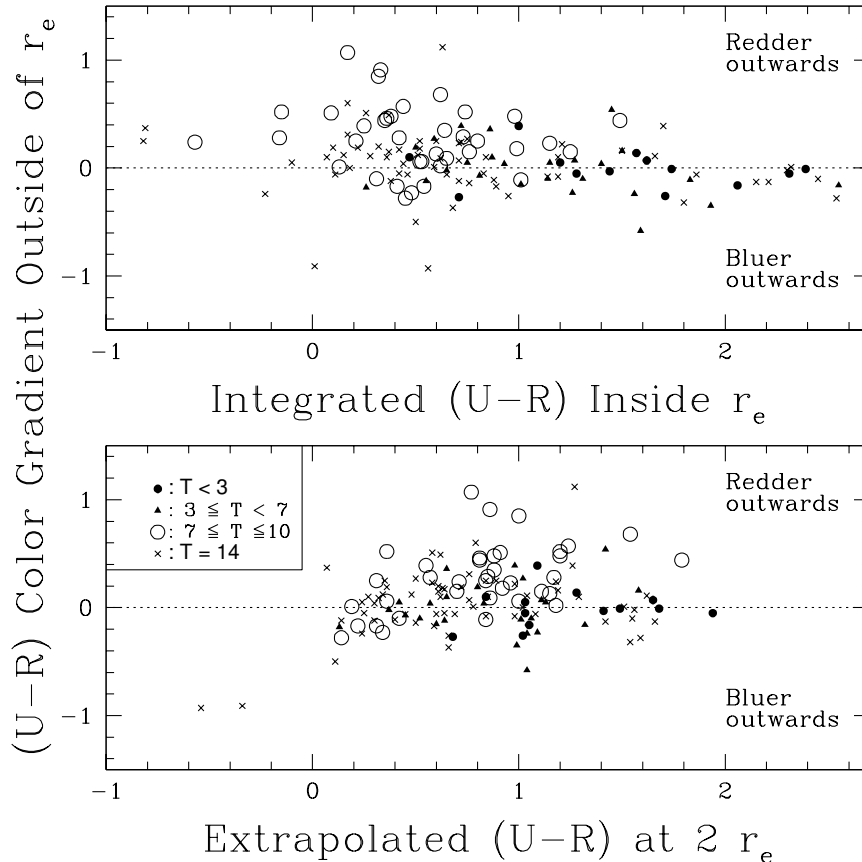


FIG. 9.— Radial  $U-R$  outer color gradient slope vs. total inner  $U-R$  color within  $r_e$  (top), and vs. outer disk color at  $2r_e$  (bottom). Different type bins are indicated with different symbols. The early-type ( $T < 3$ ), mid-type ( $3 \leq T < 7$ ), and merger/interacting ( $T = 14$ ) galaxies do not show any significant trend in inner or outer color with color slope. Late Hubble type ( $7 \leq T \leq 10$ ) galaxies also show little trend in general, although as the galaxies get redder with increasing radius, they tend to be somewhat bluer in their inner regions, and redder in their outer regions than other galaxies.

redder than to become bluer with increasing radius than galaxies that have remained unperturbed and are substantially more relaxed today. Because the merger rate at high redshift is higher, higher redshift galaxies would on average be redder with increasing radius than lower redshift galaxies, and nearby low-mass, low-luminosity, late-type and interacting galaxies would on average be redder with increasing radius than their high-mass, high-luminosity, early-type counterparts that formed predominantly at higher redshift. This scenario can therefore be tested by examining how color gradients depend on galaxy type, luminosity, and redshift.

The process of galaxy formation may be more complicated, depending in part on the galaxy’s type, luminosity, and mass, and on its surrounding environment, as discussed by Tamura & Ohta (2003), who determined that elliptical galaxies in rich galaxy clusters get bluer with increasing radius, and that larger and more luminous galaxies have steeper color gradients. These trends are consistent with models for formation through monolithic collapse (Eggen et al. 1962; Larson 1974; Carlberg 1984). In field E/SO galaxies, there is no such strong trend of color gradient with galaxy luminosity and size, which suggests that early-type galaxies in less-dense environments may form instead through hierarchical merg-

ing. Balcells & Peletier (1994) discuss the implications of early-type spiral galaxy bulge luminosity on the galaxy’s formation process. They find that bright bulges show a steeper color gradient with increasing bulge luminosity, while faint bulge color gradients become significantly bluer outward, and show no such relation with luminosity. This suggests that the brighter, more massive bulges in early-type spiral galaxies may have formed through dissipative collapse, with the presence of the disk having little effect on the the bulge’s formation. Fainter, less massive bulges, however, would have a different formation mechanism due to interactions with the disk (e.g., Kannappan et al. 2004).

Although the formation and evolution of specific galaxies may depend on various factors, our general results are consistent with the predictions of bottom-up hierarchical galaxy formation, where our more relaxed high-mass, high-luminosity, early- to mid-type galaxies become either bluer with increasing radius or have no color gradient, and our low-mass, low-luminosity late-type galaxies tend to be redder on average with increasing radius. This is in agreement with trends seen in the high redshift Universe in the Hubble Deep Field North by Moth & Elston (2002), who found that galaxies at intermediate redshifts ( $z = 0.5-1.2$ ) tend to on average get bluer with increasing radius, while high redshift galaxies ( $z = 2-3.5$ ), which are



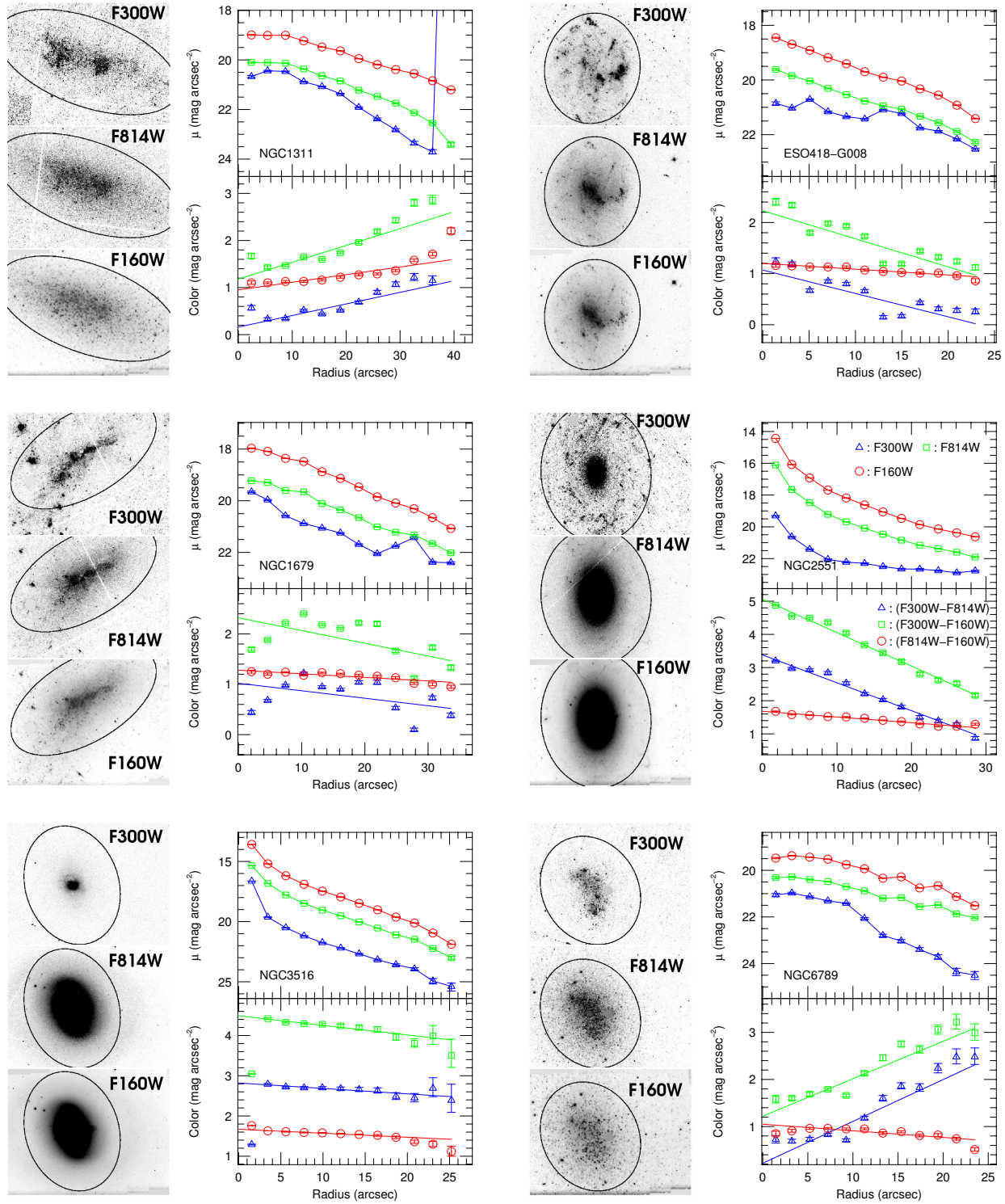


FIG. 10.— All six *HST* surface brightness ( $\mu$ ) and color profiles with images of each galaxy in all three pass-bands. The ellipse on each image marks the last annulus used in the profile calculation. Note that the images were scaled to highlight interesting galactic structure, such that existing low-surface brightness material may not be visible in these images. The upper right panel for each galaxy is the surface brightness profile, and the lower right panel is the color profile. The key printed in the NGC2551 plots apply to all of the plots. The lines in the color profile plots are the error-weighted linear-least-squares fits to all of the data points.

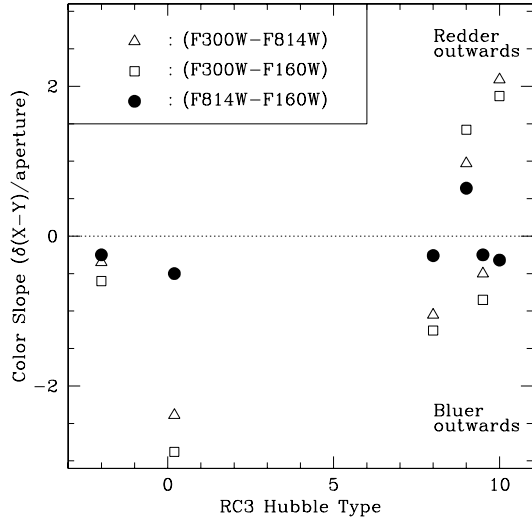


FIG. 11.— Color gradient vs. RC3 Hubble type for each of our *HST* galaxies. (F300W–F814W) and (F300W–F160W) gradients show a similar trend as the  $U$ – $R$  gradients in the VATT data, with earlier galaxy types getting bluer with increasing radius and later galaxy types either getting bluer or redder with increasing radius. The (F814W–F160W) colors get slightly bluer with increasing radius for all but one galaxy (NGC1311). For those galaxies that get bluer with radius in (F814W–F160W), the (F814W–F160W) gradients are roughly constant with Hubble type. Errors from the linear-least squares fit on the color slopes are comparable to the size of the points in this plot.

expected to be experiencing more interactions and mergers, get on average redder with increasing radius. Moth et al. (2002) determined that dust is unable to account for the strongly bluer central regions at high redshifts, and that it must therefore be due to more centrally concentrated star formation. They argue that this can be explained by hierarchical galaxy formation models, which predict that mergers and interactions are important in galaxy evolution, and more important at higher redshift. The resemblance of the color gradient trends in high redshift galaxies to those of our late-type galaxies would be consistent with the apparent similarity in morphology between high redshift galaxies and nearby irregular and peculiar galaxies. Therefore, the galaxies that most recently underwent mergers at both high and low redshift are the most likely ones to have color gradients that get significantly redder outwards, reflecting this merger.

## 6. CONCLUSIONS

We have presented images and surface brightness and color profiles for 142 mostly late-type, irregular, and peculiar galaxies observed in  $UBVR$  at the VATT. Galaxies with Hubble types earlier than Sd tend to have small color gradients (if any) and become predominantly bluer outward, consistent with the conclusions of other authors (Vader et al. 1988; Franx et al. 1989; Peletier et al. 1990; de Jong 1996; Tully et al. 1996; Jansen et al. 2000; Bell & de Jong 2000; MacArthur et al. 2004). Our late-type spiral and irregular galaxies (Sd–Im), in contrast, on average tend to become significantly redder with increasing radius from their center. We find, however, that the scatter (range) in color gradients increases toward later Hubble type, such that one can find late-type

galaxies that become somewhat bluer outward, and late-type galaxies that become much redder outward. The largest range in color gradients is found among the peculiar/interacting/merging galaxies in our sample, most of which become slightly redder outward. This particularly large scatter is consistent with the large variety of galaxy morphological types included within this class of objects, and with the complexity of the galaxy interactions.

We find that these color gradients do not have a significant dependence on the HI index, ( $M_{21} - B_T^0$ ), even though there is a trend of increasingly redder outer regions with fainter  $B_T^0$  and fainter absolute HI 21 cm emission line magnitude,  $M_{21}$ . This suggests that galaxies that are faint in all bands (which tends to be true for late-type galaxies), do become on average redder with increasing radius, but these color gradients are not necessarily caused by an excess of HI. There is also a very weak trend of redder outer regions with fainter absolute far infrared magnitude,  $M_{FIR}$ . Both of these results suggest that the increasingly strong gradients of redder colors with increasing radius in late-type galaxies may not be due to an excess of dust, but to other factors such as stellar population gradients. Other authors also conclude that these color gradients are most likely due to stellar population effects (Vader et al. 1988; de Jong 1996; Jansen et al. 2000; Bell & de Jong 2000; MacArthur et al. 2004). It would be interesting to verify this by means of a thorough study of the spatial distribution of dust in late-type galaxies.

We also analyze six galaxies observed with the Hubble Space Telescope (*HST*) with NICMOS in F160W ( $H$ ) and with WFPC2 in F300W (mid-UV) and F814W ( $I$ ). The F300W data and, hence, the (F300W–F814W) and (F300W–F160W) color gradients are sensitive to young stellar populations and star forming regions. We find that the two earlier-type galaxies become bluer with increasing radius in (F300W–F814W) and (F300W–F160W), while half of the four later-type galaxies become bluer with increasing radius, and half become redder with increasing radius. Even though there are small number statistics, the fact that this trend resembles the trend seen in the larger ground-based sample suggests that these conclusions are reasonable. Color gradients measured from the (F814W–F160W) color profile show a different trend, with all but one galaxy becoming slightly bluer with increasing radius. These small color slopes, which seem to be roughly constant with Hubble type, may be due at least in part to the fact that F814W and F160W do not sample significantly different stellar populations. This and the sensitivity of F300W on star formation may also indicate that the redder outer parts of later Hubble type galaxies may be primarily due to recent star formation concentrated near the center of these particular galaxy types, even amongst an underlying redder, older, population that becomes more dominant toward the center of the galaxy (or the degenerate possibilities of increasing metallicity or dust toward the center of the galaxy).

We propose that these color gradient trends are consistent with the trends predicted in hierarchical galaxy formation models. The tendency of nearby irregular and peculiar/merging galaxies to become on average redder with increasing radius is similar to that of high redshift galaxies. This lends some support to the theory that

high redshift galaxies are similar objects to the nearby irregular, peculiar, and merging galaxies that they resemble. A further, more detailed comparison of these nearby galaxies to high redshift galaxies is needed to more fully understand the relationship between them, which we aim to address in a future paper (Taylor et al. 2005, in prep.).

Based on observations with the VATT: the Alice P. Lennon Telescope and the Thomas J. Bannan Astrophysics Facility. This research was partially funded by

NASA grants GO-8645.01-A, GO-9124.01-A and GO-9824.01-A, awarded by STScI, which is operated by AURA for NASA under contract NAS 5-26555. Additional funding was provided by the NASA Space Grant Graduate Fellowship at ASU. We wish to thank the staff of Steward Observatory and the Vatican Advanced Technology Telescope for all of their help and support on this project. We also thank Seth Cohen for his help in classifying the galaxies presented in this work.

## REFERENCES

- Abraham, R.G., Tanvir, N.R., Santiago, B.X., Ellis, R.S., Glazebrook, K., & van den Bergh, S. 1996, *MNRAS*, 279, 47
- Balcells, M., & Peletier, R.F. 1994, *AJ*, 107, 135
- Barnes, J., & Hernquist, L. 1996, *ApJ*, 471, 115
- Bell, E.F., & de Jong, R.S. 2000, *MNRAS*, 312, 497
- Bertin, E., & Arnouts, S. 1996, *AJ*, 117, 393
- Baugh, C.M., Cole, S., Frenk, C.S., & Lacey, C.G. 1998, *ApJ*, 498, 504
- Bohlin, R.C., et al. 1991, *ApJ*, 368, 12
- Cardiel, N., Gorgas, J., Sánchez-Blázquez, P., Cenarro, A.J., Pedraz, S., Bruzual, G., & Klement, J. 2003, *A&A*, 409, 511
- Carlberg, R.G. 1984, *ApJ*, 286, 403
- Cole, S., Aragon-Salamanca, A., Frenk, C.S., Navarro, J.F., & Zepf, S.E. 1994, *MNRAS*, 271, 781
- de Grijs, R., Fritze-v. Alvensleben, U., Anders, P., Gallagher, J.S., Bastian, N., Taylor, V.A., & Windhorst, R.A. 2003, *MNRAS*, 342, 259
- de Jong, R.S. 1996, *A&A*, 313, 377
- Dekel, A., & Silk, J. 1986, *ApJ*, 303, 39
- de Vaucouleurs, G., de Vaucouleurs, A., Corwin, H. G., Buta, R.J., Paturel, G., & Fouque, P. 1991, *Third Reference Catalogue of Bright Galaxies* (Springer, New York)
- De Young, D.S. 1978, *ApJ*, 223, 47
- Driver, S.P., Windhorst, R.A., Ostrander, E.J., Keel, W.C., Griffiths, R.E., & Ratnatunga, K.U. 1995, *ApJ*, 449, L23
- Driver, S.P., Fernandez-Soto, A., Couch, W.J., Odewahn, S.C., Windhorst, R. A., Phillips, S., Lanzetta, K., & Yahil, A. 1998, *ApJ* 496, L93
- Eggen, O.J., Lynden-Bell, D., & Sandage, A.R. 1962, *ApJ*, 136, 748
- Ellis, R.S. 1997 *ARA&A*, 35, 389
- Eskridge, P.B., et al. 2003, *ApJ*, 586, 923
- Ferguson, H.C., et al. 2004, *ApJ*, 600, L107
- Friedli, D., & Benz, W. 1993, *A&A*, 268, 65
- Friedli, D., & Benz, W. 1995, *A&A*, 301, 649
- Franx, M., Illingworth, B., & Heckman, T., 1989, *AJ*, 98, 538
- Giavalisco, M., Steidel, C.C., & Macchetto, F.D. 1996, *ApJ*, 470, 189
- Glazebrook, K., Ellis, R., Santiago, B., & Griffiths, R. 1995, *MNRAS*, 275, L19
- Heckman, T.M., Armus, L., & Miley, G.K. 1990, *ApJS*, 74, 833
- Hernquist, L., & Mihos, J. 1995, *ApJ*, 448, 41
- Hibbard, J.E., & Vacca, W.D. 1997, *AJ*, 114, 1741
- Hill, J.K., et al. 1992, *ApJ*, 395, L37
- Holtzman, J.A., Burrows, C.J., Casertano, S., Hester, J.J., Trauger, J.T., Watson, A.M., & Worthey, G. 1995, *PASP*, 107, 1065
- Jansen, R.A., Franx, M., Fabricant, D., & Caldwell, N. 2000, *ApJS*, 126, 271
- Kannappan, S.J., Jansen, R.A., & Barton, E.J. 2004, *AJ*, 127, 1371
- Kauffmann, G., Nusser, A., & Steinmetz, M. 1997, *MNRAS*, 286, 795
- Kuchinski, L.E., et al. 2000, *ApJS*, 131, 441
- Landolt, A.U. 1992, *AJ*, 104, 340
- Larson, R.B. 1974, *MNRAS*, 169, 229
- Lowenthal, J.D., et al. 1997, *ApJ*, 481, 673
- MacArthur, L.A., Courteau, S., Bell, E., & Holtzman, J.A. 2004, *ApJS*, 152, 175
- Marcum, P.M., et al. 2001, *ApJS*, 132, 129
- Mathews, W. 1989, *AJ*, 97, 42
- Mihos, J., & Hernquist, L. 1994, *ApJ*, 425, L13
- Mihos, J., & Hernquist, L. 1996, *ApJ*, 464, 641
- Milliard, B., Donas, J., Laget, M., Armand, C., & Vuillemin, A. 1992, *A&A*, 257, 24
- Monet, D., et al. 1996, *USNO-SA2.0*, (U.S. Naval Observatory, Washington DC)
- Moth, P., & Elston, R.J. 2002, *AJ*, 124, 1886
- Noguchi, M. 1988, *A&A*, 203, 259
- Odewahn, S.C., Windhorst, R.A., Driver, S.P., & Keel, W.C. 1996, *ApJ*, 472, L13
- Odewahn, S.C., Cohen, S.H., Windhorst, R.A., & Philip, N.S. 2002, *ApJ*, 568, 539
- Peletier, R.F., Davies, R.L., Illingworth, G.D., Davis, L.E., & Cawson, M., 1990, *AJ*, 100, 1091
- Persson, S.E., Frogel, J.A., & Aaronson, M. 1979, *ApJS*, 39, 61
- Rhoads, J.E. 2000, *PASP*, 112, 703
- Roukema, B.F., Quinn, P.J., Peterson, B.A., & Rocca-Volmerange, B. 1997, *MNRAS*, 292, 835
- Sandage, A. 1972, *ApJ*, 176, 21
- Shlosman, I., Frank, J., & Begelman, M.C. 1989, *Nature*, 338, 45
- Shlosman, I., Begelman, M.C., & Frank, J. 1990, *Nature*, 345, 679
- Somerville, R., Primack, J.R., & Faber, S.M. 2001, *MNRAS*, 320, 504
- Tamura, N., & Ohta, K. 2003, *AJ*, 126, 596
- Taylor, V.A., Jansen, R.A., & Windhorst, R.A. 2004, *PASP*, 116, 762
- Tinsley, B.M., & Larson, R.B. 1978, *ApJ*, 221, 554
- Trujillo, I., et al. 2004, *ApJ* 604, 521
- Tully, R.B., Verheijen, M.A.W., Pierce, M.J., Huang, J., & Wainscoat, R.J. 1996, *AJ*, 112, 2471
- Vader, J.P., Vigroux, L., Lachieze-Rey, M., & Souviron, J., 1988, *A&A*, 203, 217
- Windhorst, R.A., et al. 2002, *ApJS*, 143, 113
- White, S.D.M. 1979, *MNRAS*, 189, 831
- White, S.D., & Frenk, C.S. 1991, *ApJ*, 379, 52